J. Fluid Mech. (2009), *vol.* 622, *pp.* 371–411. © 2009 Cambridge University Press
doi:10.1017/S0022112008005302 Printed in the United Kingdom

Numerical study of the effects of the breaking intensity on wave breaking flows

A. IAFRATI†
INSEAN – Italian Ship Model Basin, Rome 00128, Italy

(Received 12 February 2008 and in revised form 7 November 2008)

The flow generated by the breaking of free-surface waves of different initial steepnesses is simulated numerically. The aim is to investigate the role played by the breaking intensity on the resulting flow. The study, which assumes a two-dimensional flow, makes use of a two-fluids Navier–Stokes solver combined with a Level-Set technique for the interface capturing. The evolution of periodic wavetrains is considered. Depending on the initial steepness ε, the wavetrain remains regular or develops a breaking, which can be either of spilling or plunging type. From the analysis of the local strain fields it is shown that, in the most energetic phase of plunging breaking, dissipation is mainly localized about the small air bubbles generated by the fragmentation of the air cavity entrapped by the plunging of the jet. The downward transfer of the horizontal momentum is evaluated by integrating the flux of momentum through horizontal planes lying at different depths beneath the still water level. From weak to moderate breaking, increase in the breaking intensity results in growing transfer of horizontal momentum, as well as thickening of the surface layer. Beyond a certain breaking intensity, the larger amount of air entrapped causes a reduction in the momentum transferred and the shrinkage of the layer. Quantitative estimates of the amount of air entrapped by the breaking and of the degassing process are provided. A scaling dependence of the amount of air entrapped by the first plunging event on the initial steepness is found. A careful analysis of the circulation induced in water by the breaking process is carried out. It is seen that in the plunging regime the primary circulation induced by the breaking process scales with the velocity jump between the crest and the trough of the wave.

The limits of the main assumptions of the numerical calculations are analysed. It is shown that up to half-wave period after the breaking onset, the Reynolds number of the simulation does not significantly affect the solution. In order to further support the findings, an estimate of the uncertainty of the numerical results is derived through several repetitions of the numerical simulation with small perturbations of the initial conditions.

1. Introduction

Breaking of ocean waves is of relevant interest because of its implications in many physical, chemical and biological processes that take place at the air–water interface. Wave breaking is responsible for the generation of free-surface turbulence, dissipation of the wave energy and enhancement of the momentum, heat and gas transfer between air and water. In the naval context, the breaking of the bow wave in fast ships with

---

† Email address for correspondence: a.iafrati@insean.it

pronounced flare causes the entrapment of air bubbles that travel along the hull, eventually flowing into the wake and making it visible from high altitude radars.

The breaking of free-surface waves is characterized by a very wide range of scales. Large-scale breaking waves are characterized by strong turbulence with a significant amount of drops, spray and bubbles about the breaker front (whitecaps). At the shortest scales, the stabilizing actions of gravity and surface tension dominate over the disrupting effect of the turbulence. The development of the plunging jet is suppressed and only a small amount of air, if any, is entrained (Brocchini & Peregrine 2001). Such small-scale breaking was also called micro-breaking by Banner & Phillips (1974).

A lot of experimental studies have been done in this field. Quasi-steady breaking waves past a submerged hydrofoil were studied by Duncan (1981, 1983) in order to estimate to which extent the occurrence of breaking contributes to the wave drag and, in turn, to the energy dissipation. Rather a complete investigation of unsteady breaking waves was done by Rapp & Melville (1990). They exploited the dispersion of deep-water waves to induce breaking and used a laser Doppler technique to measure the velocity field. Through ensemble average over several repetitions of the experiment, the mean and turbulent velocity components were distinguished. It was found that the breaking significantly enhances the energy dissipation. It can be responsible for the dissipation of as much as 40 % of the initial energy content, 90 % of which is dissipated within four-wave periods after the breaking onset. In Bonmarin (1989) the time–space evolution of breaking waves was analysed with attention to the geometric properties of the free-surface profiles. Rather detailed descriptions of the splash up occurrence and of the vorticity structures originated in water as a consequence of the breaking process were provided.

The development of Particle Image Velocimetry (PIV) techniques has made more refined investigations of the flow field inside breaking waves much simpler and faster. The different patterns characterizing the wavy flow past a submerged hydrofoil when varying the Froude number were investigated by Lin & Rockwell (1995). They showed that at the lowest Froude number the solution is dominated by surface tension and is characterized by a single broad crest with no significant amount of vorticity generated. At intermediate Froude numbers the solution exhibits a capillary pattern and vorticity is mainly associated to the free-surface curvature. Further increase in the Froude number generates a quasi-steady breaker with flow separation taking place at the breaker toe. The flow field beneath quasi-steady breakers was also analysed by Dabiri & Gharib (1997) who showed that the surface current associated to the breaking is the dominant source of vorticity. A careful investigation of the unsteady development of gentle spilling breakers was done by Qiao & Duncan (2001). They showed that in the initial stage of the breaking, a bulge forms about the wave crest but no vorticity is shed. After a short while, the bulge begins to slide down along the forward face of the wave, and a shear layer develops because of the interaction between the gravity induced downslope flow near the free-surface and the underlying upslope flow of the wave.

Despite all the work done in the spilling breaking case, less is available for the unsteady development of plunging breaking. An experimental study of the velocities and accelerations originated in steep deep water waves just before the plunging breaking event was carried out by Grue & Jensen (2006). It was shown that overturning events are characterized by horizontal accelerations up to $1.1g$ and vertical acceleration up to $1.5g$, g being the acceleration of gravity. The turbulent flow generated by breaking waves in water of intermediate depth was investigated by Chang & Liu (1999). Through the ensemble average of different repeats of the same experiment, the mean and turbulent components of the flow were distinguished. The different contributions in the equation of turbulent energy budget were evaluated and it was shown that the turbulence advection, production and dissipation were equally important while the turbulent diffusion term was almost negligible. Unfortunately, owing to the light scattered by air bubbles, measurements were done only outside the aerated region. More recently, Kimmoun & Branger (2007) performed detailed PIV measurements of water waves propagating and breaking on a sloping beach and estimated the void fraction on the basis of the light intensity analysis.

In Melville, Veron & White (2002) unsteady breaking waves were generated through the same dispersive focusing technique used by Rapp & Melville (1990). A detailed description of the velocity field in a wide area about the breaking region was obtained by the reconstruction of a mosaic from tiles of PIV measurements. A careful analysis of the velocity and vorticity fields was done and an ensemble average among several repetitions of the experiment was used to distinguish the mean and the fluctuating velocity components. Also in this case, owing to the limits of the PIV technique, measurements started three-wave periods after the breaking onset, when the larger bubbles degassed. Hence, the description of flow during the most energetic phase of the breaking is missing.

The important role played by the air entrainment in the energy dissipation of breaking waves was discussed by Lamarre & Melville (1991). Through measurements of the void fraction, they showed that a large fraction of the energy dissipated by the breaking, between 30 % and 50 %, is spent against buoyancy in entrapping air bubbles. More recently, a similar experimental investigation was done by Blenkinsopp & Chaplin (2007), who showed a remarkable degree of similarity between different breaking types. Also in this case it was found that, for strong plunging breaking, at least 14 % of the energy dissipated by the breaking is spent in entraining air and generating splash.

The recent development of numerical approaches able to deal with complex free-surface flows even in the presence of significant changes in the interface topology has largely widen the use of computational tools in this context. In Scardovelli & Zaleski (1999), a survey on the different numerical techniques is provided. Of course important limitations exist owing to the high computational effort required. Direct numerical simulations are generally limited to low Reynolds numbers. Moreover, numerical simulations of two-fluids flows are often conducted using a two-dimensional assumption (Song & Sirviente 2004; Hendrickson & Yue 2006). Only recently few attempts have been made to simulate the three-dimensional wave breaking flows. Three-dimensional vortex structures generated by the breaking of a wave approaching the surf zone were investigated by Watanabe, Saeki & Hosking (2005) using a single fluid modelling. Two-fluids numerical simulations of the three-dimensional flow generated by the breaking of a two-dimensional wave were done by Lubin *et al.* (2006). Therein, the differences between two- and three-dimensional results were analysed. It was shown that the three-dimensional turbulence enhances the energy dissipation, but the differences are less than 5 % up to half-wave period after the breaking onset. The difference in the energy contents of the two- and three-dimensional simulations rises up to 10 % two and a half periods after the breaking onset and remains constant afterwards.

The above considerations explain why, in spite of the limits of the two-dimensional low-Reynolds-number numerical simulations, results obtained so far and available in literature are in reasonably good agreement with the experimental observations. The breaking of steep free-surface waves was investigated by Chen *et al.* (1999), who showed that soon after the plunging event the energy takes a t^{-1} decay trend and that a large fraction of the initial energy content is dissipated within three-wave periods after the breaking. Both results are consistent with the experimental findings by Rapp & Melville (1990) and Melville *et al.* (2002).

Because of the lack of the three-dimensional component, two-dimensional numerical simulations do not capture the interaction between the Langmuir circulation and the breaking occurrence (Thorpe 2004). Their mutual interaction plays an important role in the vertical transfer of the horizontal momentum. However, the scales at which the breaking injects momentum into the boundary layer are much shorter than those at which the interaction takes place, and the computational cost of three-dimensional numerical simulations over the entire range is still prohibitive. Instead of facing such considerable burdens, an approach of intermediate complexity was developed by Sullivan, McWilliams & Melville (2004, 2007). Rather than a detailed description of the wave breaking process, a linearized free-surface condition is used and the occurrence of breaking is modelled as a stochastic forcing term in the momentum equation. The forcing term is defined in terms of space–time shape functions which are designed in order to match the laboratory measurements. Through such numerical model, they studied the interaction between the breaking event and the Langmuir circulation and showed how the Langmuir circulation affects the momentum transfer and energy dissipation operated by the breaking process and, conversely, how the occurrence of breaking and the related vorticity is important for the generation of new Langmuir circulation. At the present stage of development, the stochastic model used in Sullivan *et al.* (2007) does not account for the air entrainment, i.e. density variations and buoyancy are not included.

What makes the two-fluids numerical model very attractive is the possibility of achieving a highly refined description of the flow field in both fluids in a non-intrusive manner. In this sense, such approaches can be of help for the definition of the forcing term in oceanic boundary layer models in the case of breaking with large amount of air entrained. Even the two-dimensional assumption is not too restrictive, as long as the interest is in the early stage after the breaking onset. This is just the stage during which large air bubbles are entrapped, making PIV measurements highly challenging.

In the present paper the two-fluids flow generated by the breaking of a two-dimensional periodic wavetrain is simulated. The numerical model is based on an unsteady two-dimensional Navier–Stokes solver for a single incompressible fluid whose physical properties vary smoothly across the interface. The free-surface between air and water is captured through a Level-Set technique (Iafrati, Di Mascio & Campana 2001). The study is carried out in a computational domain with periodic boundary conditions at the two sides, and initial conditions are essentially the same as in Chen *et al.* (1999). The main difference concerns the density ratio which, in the present work, is fixed as the real one for air and water. The initial steepness of the wavetrain is varied from low values, leading to regular waves, up to large values that give rise to strong plunging breaking.

Several aspects of the flow are investigated with particular emphasis on the changes operated by the breaking intensity. The time history of the total energy and of the viscous dissipation are analysed and the important role played by the fragmentation of the air cavity on the dissipation is highlighted. The vertical fluxes of the horizontal momentum across several horizontal planes lying at different depths is calculated and the surface current induced by the breaking process is analysed on the basis of the velocity profiles. The air entrainment and the degassing phase are qualitatively described on the basis of the free-surface profiles. Quantitative estimates of the amount of air entrapped by the breaking and of the degassing process are derived as well. A scaling law for the amount of air entrapped by the first plunging event as a function of the steepness is found. A more insightful analysis of the vorticity field and of the total circulation is presented, with particular regard to the role played by the reconnection process on the generation of vorticity. The effect of the Reynolds number on the energy dissipation and on the induced circulation is evaluated. Finally, an estimate of the uncertainty of the numerical results is achieved through the repetition of the same calculation with small perturbations of the initial conditions.

2. Numerical model

2.1. *Two-fluids Navier–Stokes solver*

The unsteady two-fluids flow of air and water induced by the breaking of free-surface waves is simulated numerically as that of a single incompressible fluid whose density and viscosity vary smoothly across the interface. With this assumption, the continuity and momentum equations given in generalized coordinates by Zang, Street & Koseff (1994) are rewritten as

$$\frac{\partial U_m}{\partial \xi_m} = 0, \tag{2.1}$$

$$\begin{aligned}\frac{\partial}{\partial t}(J^{-1}u_i) + \frac{\partial}{\partial \xi_m}(U_m u_i) = &-\frac{1}{\rho}\frac{\partial}{\partial \xi_m}\left(J^{-1}\frac{\partial \xi_m}{\partial x_i}p\right) - \frac{\kappa}{\rho\, We^2}\frac{\partial}{\partial \xi_m}\left(J^{-1}\frac{\partial \xi_m}{\partial x_i}H_{\delta_T}(d)\right)\\ &- J^{-1}\frac{\delta_{i2}}{Fr^2} + \frac{1}{\rho\, Re}\frac{\partial}{\partial \xi_m}\left(\mu G^{ml}\frac{\partial u_i}{\partial \xi_l} + \mu B^{mlji}\frac{\partial u_j}{\partial \xi_l}\right),\end{aligned} \tag{2.2}$$

respectively, where the variation of density and viscosity across the computational domain is accounted for (Iafrati & Campana 2003). In the above equations u_i is the ith Cartesian velocity component, δ_{ij} is the Kronecker delta,

$$U_m = J^{-1}\frac{\partial \xi_m}{\partial x_j}u_j \tag{2.3}$$

is the volume flux through the ξ_m surface and J^{-1} is the inverse of the Jacobian. Non-dimensional ratios are defined as

$$Fr = \frac{U_r}{\sqrt{gL_r}}, \quad Re = \frac{U_r L_r \rho_w}{\mu_w}, \quad We = U_r\sqrt{\frac{\rho_w L_r}{\sigma}} \tag{2.4}$$

for Froude, Reynolds and Weber numbers, respectively. Here, U_r and L_r are reference values for velocity and length, σ is the surface tension coefficient, ρ_w and μ_w are the density and dynamic viscosity of water, respectively, which are also assumed as reference values. Surface tension effects are modelled as a continuum force acting on a thin layer about the air–water interface (Brackbill, Kothe & Zemach 1992). Functionally, this is expressed as the gradient of the smoothed Heaviside function

$$H_\delta(d) = \begin{cases} \dfrac{1}{2} + \dfrac{1}{2}\sin\left(\dfrac{\pi d}{2\delta}\right) & \text{for } |d| \leqslant \delta \\ 0 & \text{for } d < -\delta \\ 1 & \text{for } d > +\delta \end{cases} \tag{2.5}$$

with d denoting the signed distance from the interface, taken positive in water and negative in air. In the surface tension contribution to the momentum equation (2.2), the smoothed Heaviside function (2.5) is used with $\delta = \delta_T$, where δ_T is half of the thickness of the region across which surface tension forces are spread.

Finally, in (2.2)

$$G^{ml} = J^{-1}\frac{\partial \xi_m}{\partial x_j}\frac{\partial \xi_l}{\partial x_j} \qquad B^{mlji} = J^{-1}\frac{\partial \xi_m}{\partial x_j}\frac{\partial \xi_l}{\partial x_i}$$

are metric quantities and κ is the local curvature.

The numerical solution of the system of Navier–Stokes equations is achieved through a non-staggered collocation of variables: Cartesian velocities and pressure are defined at the cell centres, whereas volume fluxes are defined at the mid-point of the cell faces (Zang *et al.* 1994). The system is integrated in time with a fractional step approach: the pressure contribution is neglected when integrating the momentum equation in time (*Predictor step*) and it is reintroduced next when the continuity of the velocity field is enforced (*Corrector step*). The diagonal part of the first viscous contribution in (2.2) is computed implicitly with a Crank–Nicolson scheme with the aim of avoiding the constraints of the corresponding stability limit. All other terms are computed explicitly with a three-steps low storage Runge–Kutta scheme (Rai & Moin 1991). The grid being fixed in time, the discretized form of the momentum equation at the step n is

(*a*) *Sub-step 1*

$$\begin{aligned}(J^{-1} - \alpha_1 \Delta t D_I)\frac{(\hat{u}_i^1 - u_i^n)}{\Delta t} &= \gamma_1\left[C\left(u_i^n\right) + D_E\left(u_i^n\right) + T_i(d^n)\right] \\ &\quad + 2\alpha_1\left[-J^{-1}\frac{\delta_{i2}}{Fr^2} + D_I\left(u_i^n\right)\right],\end{aligned}$$

$$\tilde{u}_i^1 - \hat{u}_i^1 = \gamma_1 \frac{R_i(\tilde{\phi}^1)}{\tilde{\rho}^1 J^{-1}}$$

(*b*) *Sub-step 2*

$$\begin{aligned}(J^{-1} - \alpha_2 \Delta t D_I)\frac{(\hat{u}_i^2 - \tilde{u}_i^1)}{\Delta t} &= \gamma_2\left[C\left(\tilde{u}_i^1\right) + D_E\left(\tilde{u}_i^1\right) + T_i(\tilde{d}^1)\right] \\ &\quad + \zeta_1\left[C\left(u_i^n\right) + D_E\left(u_i^n\right) + T_i(d^n)\right] \\ &\quad + 2\alpha_2\left[-J^{-1}\frac{\delta_{i2}}{Fr^2} + D_I\left(\tilde{u}_i^1\right)\right],\end{aligned}$$

$$\tilde{u}_i^2 - \hat{u}_i^2 = \gamma_2 \frac{R_i(\tilde{\phi}^2)}{\tilde{\rho}^2 J^{-1}} + \zeta_1 \frac{R_i(\tilde{\phi}^1)}{\tilde{\rho}^1 J^{-1}}$$

(*c*) *Sub-step 3*

$$\begin{aligned}(J^{-1} - \alpha_3 \Delta t D_I)\frac{(\hat{u}_i^3 - \tilde{u}_i^2)}{\Delta t} &= \gamma_3\left[C\left(\tilde{u}_i^2\right) + D_E\left(\tilde{u}_i^2\right) + T_i(\tilde{d}^2)\right] \\ &\quad + \zeta_2\left[C\left(\tilde{u}_i^1\right) + D_E\left(\tilde{u}_i^1\right) + T_i(\tilde{d}^1)\right] \\ &\quad + 2\alpha_3\left[-J^{-1}\frac{\delta_{i2}}{Fr^2} + D_I\left(\tilde{u}_i^2\right)\right],\end{aligned}$$

$$u_i^{n+1} - \hat{u}_i^3 = \gamma_3 \frac{R_i(\phi^{n+1})}{\rho^{n+1} J^{-1}} + \zeta_2 \frac{R_i(\tilde{\phi}^2)}{\tilde{\rho}^2 J^{-1}}.$$

The coefficients α_i, γ_i and ζ_i are reported in Rai & Moin (1991) and in literature cited therein. In the above equations, for the sake of clarity, a compact notation is used for the convective, diffusive and surface tension contributions:

$$
\begin{aligned}
C(u_i) &= -\frac{\partial}{\partial \xi_m}(U_m u_i), \\
D_I(u_i) &= \frac{1}{\rho\, Re}\frac{\partial}{\partial \xi_m}\left(\mu G^{ml}\frac{\partial u_i}{\partial \xi_l}\right), \qquad m = l, \\
D_E(u_i) &= \frac{1}{\rho\, Re}\frac{\partial}{\partial \xi_l}\left(\mu G^{ml}\frac{\partial u_i}{\partial \xi_l} + \mu B^{mkji}\frac{\partial u_j}{\partial \xi_k}\right), \qquad m \neq l, \\
T_i(d) &= -\frac{\kappa}{\rho We^2}\frac{\partial}{\partial \xi_m}\left(J^{-1}\frac{\partial \xi_m}{\partial x_i}H_{\delta_T}(d)\right)
\end{aligned}
$$

and

$$
R_i(f) = -\frac{\partial}{\partial \xi_m}\left(J^{-1}\frac{\partial \xi_m}{\partial x_i} f\right) \tag{2.6}
$$

indicates the gradient operator in generalized coordinates.

The pressure corrector ϕ is found by enforcing the continuity of the velocity field at the end of the predictor sub-step (Chorin 1967; Kim & Moin 1985). Once the auxiliary velocity field is found, say $\hat{u}_i^l$, the fluxes $\hat{U}_m^l$ at the mid-point of the cell faces associated to this velocity field are computed through (2.3). Cartesian velocity components at the mid-point of the cell faces are obtained by a quadratic upwind interpolation of the values at the cell centres. In terms of fluxes, the corrector step can be written as

$$
\tilde{U}_m^l - \hat{U}_m^l = -\gamma_l \Delta t\left(\frac{G^{mj}}{\tilde{\rho}^l}\frac{\partial \tilde{\phi}^l}{\partial \xi_j}\right) - \zeta_{l-1}\Delta t\left(\frac{G^{mj}}{\tilde{\rho}^{l-1}}\frac{\partial \tilde{\phi}^{l-1}}{\partial \xi_j}\right), \tag{2.7}
$$

and, by enforcing the continuity equation (2.1) to $\tilde{U}_m^l$, the following Poisson equation for the pressure corrector is obtained:

$$
\frac{\partial}{\partial \xi_m}\left(\frac{G^{mj}}{\tilde{\rho}^l}\frac{\partial \tilde{\phi}^l}{\partial \xi_j}\right) = \frac{1}{\Delta t}\frac{\partial \hat{U}_m^l}{\partial \xi_m} - \frac{\zeta_{l-1}}{\gamma_l}\frac{\partial}{\partial \xi_m}\left(\frac{G^{mj}}{\tilde{\rho}^{l-1}}\frac{\partial \tilde{\phi}^{l-1}}{\partial \xi_j}\right). \tag{2.8}
$$

When the velocity field is assigned throughout the boundary of the computational domain, (2.7) provides Neumann boundary conditions for the Poisson equation (2.8). The pressure field is related to the pressure corrector term by the equation:

$$
R_i(\tilde{p}^l) = (\tilde{\rho}^l J^{-1} - \alpha_l \Delta t D_I)\left(\frac{R_i(\tilde{\phi}^l)}{\tilde{\rho}^l J^{-1}}\right), \tag{2.9}
$$

solution of which in generalized coordinates is not straightforward. For this reason an approximate estimate of the pressure field is usually derived as (Rosenfeld, Kwak & Vinokur 1991)

$$
R_i(\tilde{p}^l) \simeq R_i(\tilde{\phi}^l) \;\Rightarrow\; \tilde{p}^l = \tilde{\phi}^l + O(\Delta t). \tag{2.10}
$$

As the pressure field is not used in the numerical calculation, this choice does not affect the second-order accuracy of the time integration of the system of differential equations.

The time step is adjusted so that the maximum Courant number is 1.5, below the upper limit allowed by the three-steps Runge–Kutta which is $\sqrt{3}$. However, an additional constraint to the time step

$$\Delta t < We\sqrt{\frac{(1+\rho_a/\rho_w)}{4\pi}\Delta x^3}$$

arises from the use of an explicit scheme for the surface tension effects (Brackbill *et al.* 1992) and further limitations may also be necessary as not all of the viscous contributions are treated implicitly.

Equation (2.8) is discretized by using a second-order accurate centred scheme. Owing to the large density jump occurring at the interface, the corresponding linear system is highly ill conditioned and this makes the solution of the Poisson equation very challenging and time demanding. The system is preconditioned by an incomplete LU decomposition and it is solved through a biconjugate gradient stabilized (BiCGstab) algorithm (van der Vorst 1992).

2.2. *Interface capturing technique*

The distribution of density and viscosity inside the fluid domain are given as a function of the signed distance from the interface d according to the equation

$$f(d) = f_a + (f_w - f_a)H_{\delta_P}(d), \tag{2.11}$$

where the parameter δ_P is half of the thickness of the region across which the density and viscosity jumps are spread. In the numerical calculations the parameter δ_P is chosen so that the density and viscosity jumps are spread across at least five-grid cells. Detailed studies of the role played by δ_T and δ_P on the free-surface dynamics are provided in Iafrati *et al.* (2001) and Iafrati & Campana (2005).

The free-surface motion is described with a Level-Set approach (Sussman, Smereka & Osher 1994). At the beginning of the time step the function $d(\boldsymbol{x}, t)$ is initialized as the signed normal distance from the interface, with $d > 0$ in water and $d < 0$ in air. The function d is advected in time with the flow as a non-diffusive scalar using the equation

$$\frac{\partial d}{\partial t} + \boldsymbol{u}\cdot\nabla d = 0, \tag{2.12}$$

and, according to the kinematic condition, at the end of each time step the interface is located as the zero level of the updated field $d(\boldsymbol{x}, t + \Delta t)$. The transport equation (2.12) is discretized with the same scheme adopted for the convective terms, and integrated in time through the three-steps Runge–Kutta, thus obtaining

$$\hat{d}^l = \tilde{d}^{l-1} + \gamma_l \Delta t C(\tilde{d}^{l-1}) + \zeta_{l-1}\Delta t C(\tilde{d}^{l-2}) \tag{2.13}$$

with $\tilde{d}^0 \equiv d^n$, $\tilde{d}^3 \equiv d^{n+1}$ and

$$C(\tilde{d}^l) = -\frac{\partial}{\partial \xi_m}\left(\tilde{U}^l_m \tilde{d}^l\right).$$

As the function d is defined at the cell centres, in discrete form the interface is reconstructed by locating the $d = 0$ level within the cells of the staggered grid built on the cell centres. A bilinear interpolation of the values the function d takes at the four nodes of the cell is used for this purpose. Although this choice implies the interface reconstruction being only first-order accurate in space, it allows the identification of interface portion inside one cell without involving the values the function d takes at the nodes of the contiguous ones. This approach makes the reconstruction procedure very simple even in the presence of complex interface topologies.

For the interface reconstruction, the model first seeks the intersections of the $d = 0$ level with the faces of the staggered cell. Of course, if the function d takes the same sign at the four nodes of the cell, there are no intersections. This implies that closed $d = 0$ contours smaller than one grid cell or filaments thinner than the cell size cannot be represented. The intersections between the interface and the cell faces are located through a linear interpolation of the values the function takes at the two nodes of the face. If only two intersections with the cell boundary are found, a bilinear interpolation of the values taken at the four nodes is built and exploited to locate an additional intersection point inside the cell. In this case the interface portion lying inside the cell is described by two adjacent segments. When four sign changes are found moving along the cell boundary, four intersections with the cell faces can be identified, thus giving rise to two disjoint interface segments (Iafrati & Campana 2003).

When the new interface configuration is reconstructed, the function d is reinitialized by computing at each cell centre the minimum distance from the set of interface segments. In order to avoid the artificial motion of the interface during the reinitialization, the distance function is not reinitialized on the nodes belonging to cells crossed by the interface. More details about the reinitialization procedure are given in Iafrati *et al.* (2001) and Iafrati & Campana (2003). In the latter the effect of the grid spacing and of the thickness of the transition region on the mass conservation are discussed as well.

As discussed in § 3.5, in numerical simulations of breaking waves mass conservation is made very challenging by the fragmentation of the entrapped air cavity into small air bubbles and filaments. When dimensions of bubbles or filaments become comparable to the grid spacing, those structures disappear and the corresponding area is filled by water. The only possibility of achieving a good conservation of mass together with an accurate description of the dynamics of the smallest bubbles is to use interface tracking approaches in which the interface is followed in a Lagrangian way (Unverdi & Tryggvason 1992). However, in those methods the handling of changes in the interface topology is rather complicated.

The most interesting aspect of interface capturing methods lies in their capability of dealing with changes in the topology. As discussed in Iafrati & Campana (2005), in the level-set approach the interface topology changes as a consequence of a variation of the topology of the subsets where d takes positive and negative signs. This variation implicitly occurs during the integration in time of the transport equation (2.12) although the change in the topology becomes evident only when the new interface configuration is reconstructed from the new distribution of the distance function.

Once the distance function is reinitialized the local density and viscosity values are given by (2.11). Due to the smoothing of the step function across the $d = 0$ level, a layer of intermediate density and viscosity exists nearby the interface. As a consequence, pure air (or pure water) density can be found in bubbles (or drops) only if their thickness is larger than $2\delta_P$. Below that size, bubbles or drops cannot be considered as fully resolved.

3. Effect of the steepness on wave breaking flows

3.1. *Initial free-surface shape and velocity field*

A periodic wavetrain is initialized, evolution of which is simulated numerically in a computational domain with periodic boundary conditions at the two sides. As in Chen *et al.* (1999), the initial free-surface profile is assigned as a wave in infinite depth calculated up to the third order in the wave amplitude a, that is

$$\eta(x) = \frac{a}{\lambda}\left(\cos(kx) + \frac{1}{2}\varepsilon\cos(2kx) + \frac{3}{8}\varepsilon^2\cos(3kx)\right), \tag{3.1}$$

where $k = 2\pi/\lambda$ is the fundamental wavenumber, $\varepsilon = ak$ the initial wave steepness and λ the fundamental wavelength. The wavelength λ is taken as reference value for lengths whereas $U_r = \sqrt{\lambda g}$ is assumed as reference value for the velocities. The initial velocity field in water is derived from the velocity potential related to the free-surface profile (3.1), which is

$$u = \Omega a \exp(ky)\cos(kx), \qquad v = \Omega a \exp(ky)\sin(kx), \tag{3.2}$$

where $\Omega = \sqrt{gk(1+\varepsilon^2)}$ accounts for the nonlinear correction (Whitham 1974). It is worth remarking that (3.1) does not exactly represent a third-order Stokes wave as the secular term is missing (Grue *et al.* 2003). The purpose of the present paper is to generate breaking of different intensities and to investigate the resulting flow. In this regard the lack of the secular term has only a minor effect on the results presented, as discussed later on.

At the beginning of the simulation the fluid is assumed to be at rest in the air domain, and the motion occurring in air in the later stage is induced by the momentum exchange at the interface operated by both tangential and normal stresses. No-slip boundary conditions are assigned at the top and bottom boundaries. As the water depth is of the order of half of the fundamental wavelength, this choice does not affect remarkably the dynamics of the breaking process (Chen *et al.* 1999). Also, for such wavelength–depth ratio, the energy loss by bottom friction is essentially negligible (Lighthill 1978).

In order to investigate to which extent the initial wave steepness changes the phenomena involved in the breaking event, numerical simulations are carried out by varying ε in the range 0.2–0.65. In all cases it is assumed

$$We = g^{1/2}\lambda\sqrt{\frac{\rho_w}{\sigma}} = 100,$$

which corresponds to water waves of about 30 cm wavelength. At such wavelength the Reynolds number is

$$Re = \frac{\rho_w g^{1/2}\lambda^{3/2}}{\mu_w} \simeq 4.4 \times 10^5.$$

Even in the two-dimensional case, numerical simulations of flows at such high Reynolds number would require a very large computational effort for all the relevant scales of the flow to be resolved. For this reason numerical simulations are carried out at $Re = 10^4$. Only in the case $\varepsilon = 0.55$ the numerical simulation is repeated using $Re = 10^5$ and comparisons are established in order to analyse the role played by the Reynolds number on several aspects of the resulting flow.

The density ratio is assumed to be equal to the real one for air and water, which is $\rho_a/\rho_w = 0.00125$, whereas the viscosity ratio $\mu_a/\mu_w = 0.04$, the same used in Chen *et al.* (1999). The computational domain is one fundamental wavelength wide and one fundamental wavelength high, that is $x, y \in [-0.5, 0.5]$, and it is discretized by 512×512 grid cells, uniformly spaced. For the largest steepness, $\varepsilon = 0.65$, large drops with high upward velocity components are generated by the plunging of the jet. Therefore, a higher computational domain, with $y \in [-0.5, 1.5]$ and a 512×1024

ε	Re	$N_x \times N_y$	$(x_{\min}, x_{\max}) \times (y_{\min}, y_{\max})$	$\delta_P = \delta_T$
0.2/0.60	10^4	512×512	$(-0.5, 0.5) \times (-0.5 \times 0.5)$	0.005
0.65	10^4	512×1024	$(-0.5, 0.5) \times (-0.5 \times 1.5)$	0.005
0.55	10^5	1024×1024	$(-0.5, 0.5) \times (-0.5 \times 0.5)$	0.005

TABLE 1. Parameters used for the numerical simulations.

grid, is used to prevent the motion of the drops to be strongly affected by the upper boundary. In the numerical simulations it is assumed $\delta_P = \delta_T = 0.005$ which means that density and viscosity jumps and surface tension forces are spread across a region which is about five grid cells thick. As lengths are scaled by the wavelength, for a 30 cm wave such thickness corresponds to 3 mm. For the sake of the clarity, the parameters of the simulations are given in table 1.

A 1024×1024 grid is used for the numerical simulation at $Re = 10^5$ with the aim of achieving a better description of the smaller scales expected. The same values for the thickness of the transition region $\delta_P = \delta_T = 0.005$ are adopted though. This is needed in order to have a larger number of grid points inside the transition layer, which prevent the development of spurious instabilities. It is worth remarking that this discretization is not enough to resolve the finest details of the flow at such high Reynolds number. However, the comparisons with results obtained with a coarser grid, not shown here, indicate that a satisfactory agreement is achieved at least in terms of global quantities like total energy and circulations in the early stage after the breaking onset. In a later stage of the process, it is expected that smaller scales, as well as three-dimensional effects neglected here, become more important in governing the turbulence.

With the aim of deriving an estimate of the uncertainty in the numerical results, for the case with $\varepsilon = 0.60$, several repetitions of the simulation are carried out by introducing small perturbations to the initial conditions. In some sense, this attempts to mimic what usually happens in the experiments where, due to the residual turbulence level and/or small perturbations in the initial free-surface profile, differences in the breaking dynamics occur, although the main features are well repeatable. If the present numerical model is used with the same initial and boundary conditions, it generates exactly the same results. Therefore, the initial boundary conditions are artificially perturbed by introducing a small shift to the argument in the initial conditions (3.1) and (3.2). The shift, which is a fraction of the cell size Δx, is enforced by replacing the argument x with $x - r\Delta x$, so that (3.1) and (3.2) become

$$\eta(x) = \frac{a}{\lambda}\left[\cos(k(x - r\Delta x)) + \frac{1}{2}\varepsilon\cos(2k(x - r\Delta x)) + \frac{3}{8}\varepsilon^2\cos(3k(x - r\Delta x))\right], \quad (3.3)$$

$$u = \Omega a \exp(ky)\cos(k(x - r\Delta x)), \qquad v = \Omega a \exp(ky)\sin(k(x - r\Delta x)), \quad (3.4)$$

where $r \in (0, 1)$ is a randomly assigned coefficient.

3.2. *Free-surface dynamics and vorticity production*

The analysis of the interface evolution is the simplest and the most efficient tool for illustrating the way the increasing steepness alters the wave dynamics. As indicated in table 2, the wavetrain remains regular for $\varepsilon = 0.2$ and 0.3 and breaks for $\varepsilon \geqslant 0.33$. The breaking is of the spilling type for $\varepsilon = 0.33$ and 0.35 whereas it is of the plunging type for $\varepsilon \geqslant 0.37$. The above results agrees with the analysis done by Grue & Fructus (in press), who showed that the maximum steepness for non-breaking third-order

ε	Regular	Spilling	Plunging
0.20	X		
0.30	X		
0.33		X	
0.35		X	
0.37			X
0.40			X
0.50			X
0.55			X
0.60			X
0.65			X

TABLE 2. Breaking type at different steepnesses.

Stokes wave is $\tilde{\varepsilon} = 0.32$ which corresponds to $\varepsilon \simeq 0.324$ if the secular term $\tilde{\varepsilon}^3/8$ is accounted for.

In figure 1 the sequences of the free-surface profiles obtained for different values of the initial wave steepness are drawn. In the breaking cases, the sequences show the progressive steepening of the wave profile, followed by the breaking event. At short wavelengths, surface tension plays an important role contrasting the effects of gravity and inertia at the free surface. For small amplitude breaking waves, the velocity of the jet tip is not strong enough and thus surface tension forces prevent the formation of the jet which is replaced by a bulge developing about the wave crest. After a short time the bulge begins a rapid motion down along the forward face of the wave and the breaking results to be of the spilling type (Duncan *et al.* 1999). It is expected that surface tension effects also generate capillary ripples in front of the breaker toe. On the basis of the experimental measurements reported in Diorio, Liu & Duncan (2008), at such wavelength the maximum thickness of the first capillary ripple is less than 0.7 mm, which is poorly resolved by the adopted discretization.

For larger wave amplitudes, surface tension forces can only round the tip of the jet but are not enough to avoid its formation (Brocchini & Peregrine 2001). The jet plunges onto the free surface ahead, entrapping a large air cavity and leading to a splash up formation. Then, in a sort of cascade, there are new jet impacts and other air cavities are entrapped with a progressive reduction of the sizes. Next, the entrapped air cavities collapse and fragment into smaller bubbles that slowly rise back towards the free-surface owing to the action of the buoyancy, eventually escaping out of the water. The sequences also show that the increase in the initial wave steepness anticipates the first breaking event and makes the intensity of the breaking stronger. Due to the stronger breaking, the entrapped air cavities grow in size and last longer, as it is clearly displayed by figure 1(c, d). A more detailed and quantitative analysis of the air entrainment and of the degassing process is provided in § 3.5.

A more careful look of the free-surface profiles drawn in figure 1(d) indicates that the first plunging event takes place about $t = 2.6$ and the second event occurs about $t = 4.8$. As shown in the next section, such double event is related to the presence of a standing wave component associated to the initial conditions. This point is discussed in further detail in § 3.5 where the occurrence of sudden changes in the area of the entrapped air are analysed in relation with the corresponding free-surface profiles (see figure 20).

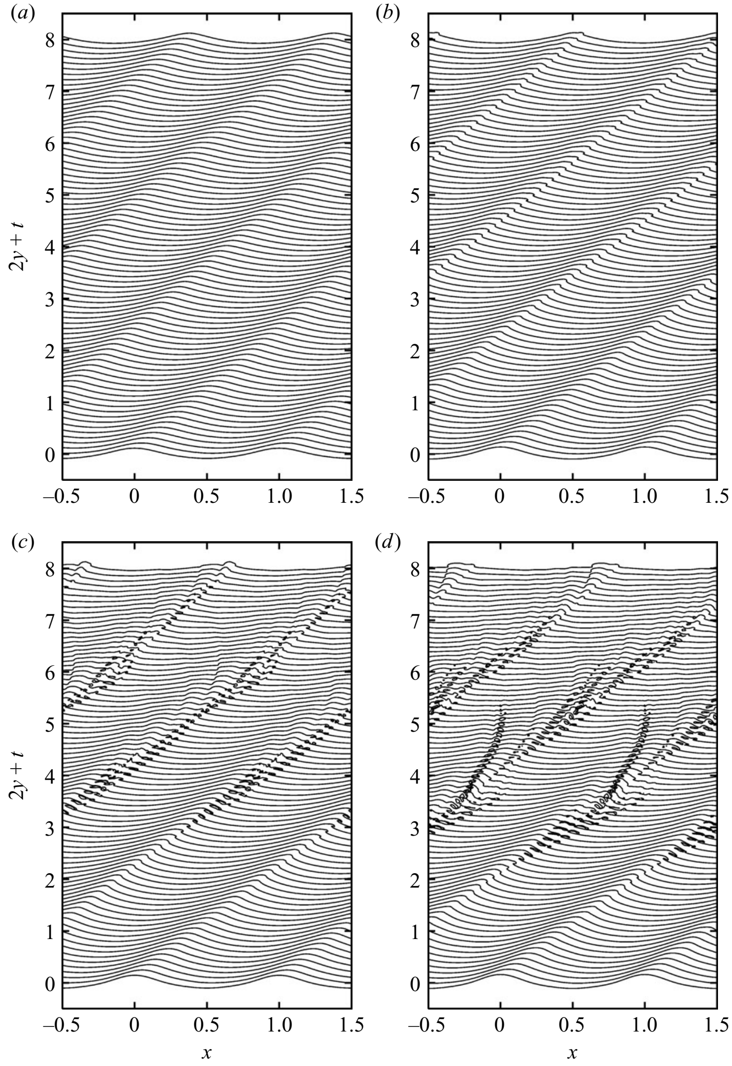

FIGURE 1. Sequences of the free-surface profiles obtained for growing initial wave steepness: (*a*) $\varepsilon = 0.3$, (*b*) $\varepsilon = 0.35$, (*c*) $\varepsilon = 0.37$ and (*d*) $\varepsilon = 0.4$. In order to help the understanding of the interface dynamics, profiles are also drawn in the interval $x \in [0.5, 1.5]$ by adding a horizontal displacement to the computed results. The vertical coordinate is multiplied by a factor two and a vertical shift equal to the corresponding time instant is also applied at each profile.

The different breaking types are characterized by different vorticity production mechanisms, as it can be seen from figure 2 where the free-surface profiles and the vorticity contours are drawn for $\varepsilon = 0.35$ and 0.6. In the spilling breaking case vorticity is mainly generated by viscous effects which induce the flow separation at the toe and give rise to the shear layer. Instabilities of the shear layer may eventually lead to the formation of large coherent structures which interact with the free-surface and produce downstream propagating fluctuations, as it was shown experimentally by Qiao & Duncan (2001) and numerically by Iafrati & Campana (2005).

In the plunging breaking case, due to the impact of the jet onto the free surface, a large air cavity is entrapped which is first convected downward and

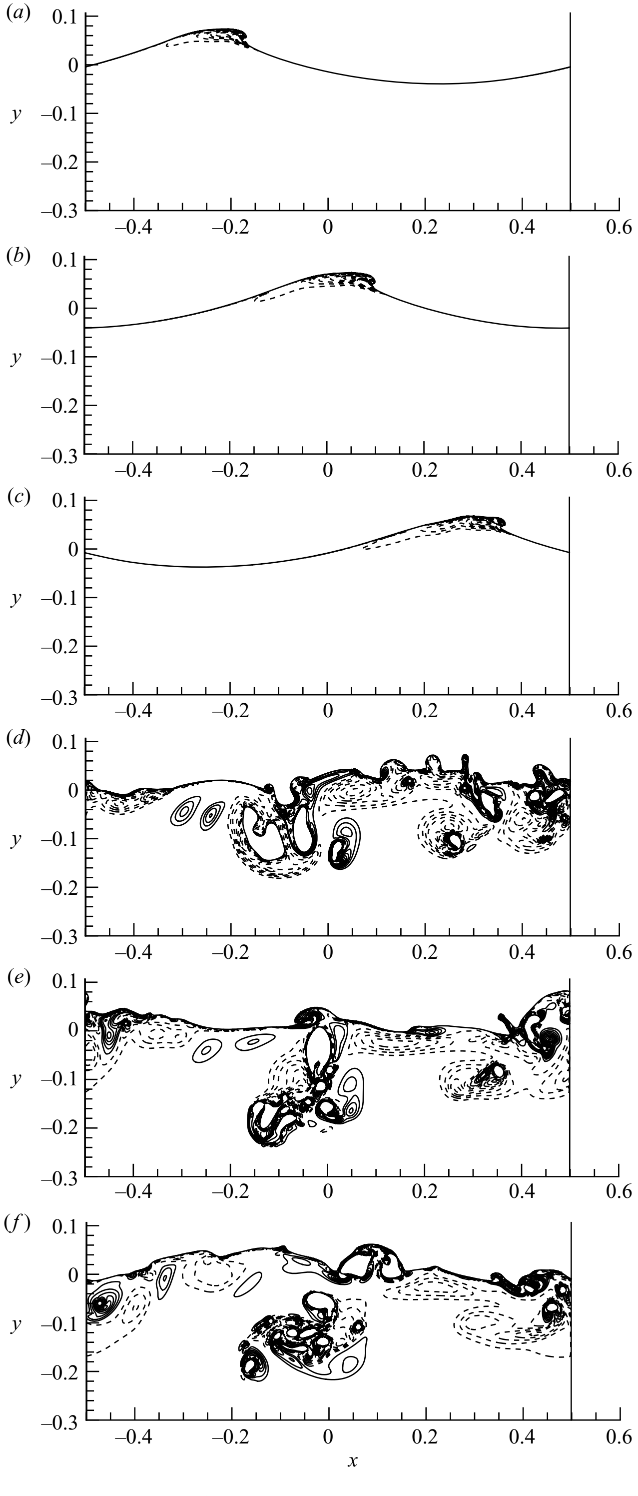

FIGURE 2. Free-surface profiles and vorticity contours at $t = 4.0, 4.6$ and 5.2 for $\varepsilon = 0.35$ (a, b, c) and $\varepsilon = 0.60$ (d, e, f). Dashed lines are used for clockwise vorticity. Vorticity contours are drawn from -15 to $+15$ with isocurve step $\Delta\omega = 1.5$.

then progressively squeezed and eventually fragmented into smaller ones. Next, the bubbles are gradually pushed back towards the free surface by the effect of both velocity field and buoyancy. The bubble distribution and the fragmentation process of the air cavity entrapped by breaking waves were investigated by Deane & Stokes (2002). They showed that the fragmentation process governs the bubble size distribution up to bubbles larger than 1 mm. Bubbles smaller than that size are stabilized by surface tension forces and do not fragment. Although their results refer to a longer wavelength, about 2.3 m, and to a higher Reynolds number, it is worth establishing a connection between the numerical results and the experimental measurements. As aforementioned, the physical size of the cell used in the present simulations is about 0.6 mm, but due to the use of the transition region for the density, bubbles smaller than 3 mm cannot be considered as fully resolved. Because of this limit in the resolution, it is expected that the fragmentation process continues a little beyond the present results at least for the simulation at higher Reynolds number.

The plunging of the jet and the closure of the cavity generate a strong clockwise rotating flow in water. The viscous interaction of these primary vorticity structures with the surrounding fluid and the interaction with the free surface induce secondary vorticity structures of opposite sign. Counter-clockwise rotating vorticity is also generated by the closure of the cavity lying on the forward face of the jet and by the plunging of backward propagating fronts (figure 24). The generation of the strong rotational flow in water due to the plunging of the jet and the occurrence of secondary vorticity structures were clearly explained by Bonmarin (1989) on the basis of experimental observations. The rotational velocity field about the entrapped air bubbles is displayed in figure 2(d, e, f).

It is worth remarking that the use of a smooth variation for the fluid density and of the continuum model for the surface tension introduces spurious velocity and vorticity components inside the transition layer. In order to evaluate to which extent the spurious effects influence the solution, a careful validation and verification study was performed in Iafrati & Campana (2005). Comparisons with results obtained by Ohring & Lugt (1991) through a single-fluid boundary-fitted approach were established. Concerning with the smooth variation of the fluid properties, the study showed that spurious effects remain confined inside the transition layer and do not affect the solution outside, provided that the layer is at least five cells thick. As discussed above, the minimum number of grid cells inside the transition region has to be larger for simulations at higher Reynolds numbers. For the surface tension model, it was found that accurate results can be achieved if the thickness of the layer is not too wide compared to the local radius of curvature of the interface. On the other hand, the thickness of the layer cannot be too small than, say, five grid cells in order to ensure a correct evaluation of the interface curvature through numerical differentiation of the smoothed Heaviside function.

In addition to the vorticity structures generated at the first jet impact, viscous effects at the free surface induces vorticity also in a later stage. For instance, this is the case when primary or secondary structures rise back and interact with the air–water interface, as it can be seen in figure 2(e) about $x = 0.2$. Such a viscous interaction generates counter-rotating vortices and a cusp-like free-surface shape where small air bubbles may eventually be entrapped. The entrainment of air bubbles caused by the interaction of counter-rotating vortex structures with the free surface was illustrated by Bonmarin (1989). The importance of the vorticity–free-surface interaction and the surface renewal processes in the enhancement of the heat and gas transfer between air

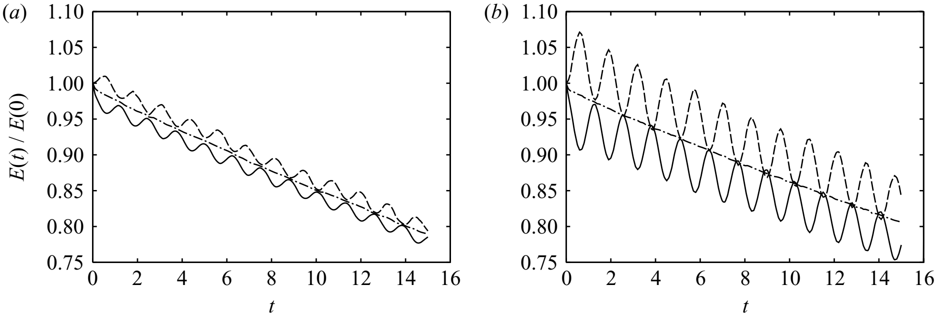

FIGURE 3. Time histories of the kinetic (solid), potential (dash) and total (dash-dot) energy for the two non-breaking cases: (*a*) $\varepsilon = 0.2$ and (*b*) $\varepsilon = 0.3$. All quantities are non-dimensionalized by the corresponding initial value.

and water were investigated by Siddiqui *et al.* (2001, 2004) in the field of microscale breaking waves generated by the wind–water interaction.

3.3. *Role of breaking occurrence on energy dissipation*

With the aim of investigating the energy decay processes and the role played by the breaking on that regard, the kinetic and potential energy are evaluated as

$$E_K = \frac{1}{2}\int_{d\geqslant 0} \rho(u^2+v^2)\,\mathrm{d}x\,\mathrm{d}y, \qquad E_P = \int_{d\geqslant 0} \rho y\,\mathrm{d}x\,\mathrm{d}y + \frac{1}{8}, \tag{3.5}$$

respectively, with the constant term 1/8 in the last equation introduced to get zero potential energy for the flat free surface. The integrals in (3.5) are taken over the domain with a positive distance from the interface, which is the nominal water domain. It is worth noticing that, due to the high Weber number of the numerical simulations, the surface tension contribution to the energy balance is negligible and is not considered in the following analysis (Chen *et al.* 1999). The total mechanical energy of the wave is obtained as the sum of the kinetic and potential contributions $E_T = E_K + E_P$.

The time histories of the kinetic, potential and total energies for the two non-breaking cases, i.e. $\varepsilon = 0.2$ and 0.3, are drawn in figure 3. Data are non-dimensionalized by the corresponding initial values. The time histories of the kinetic and potential energies exhibit oscillating components of the same amplitude, opposite phase and a period of order of 1.28. Per linear theory, the period of the fundamental wave component is approximately $T = \sqrt{2\pi} \simeq 2.5$, which is about twice the period of the oscillating components of the kinetic and potential energies. The behaviour is consistent with the presence of a standing wave component, of the same wavelength as that of the fundamental one, superimposed to the progressive wave system. The comparison of the results obtained for the two different initial steepnesses also indicates that, relatively speaking, the amount of energy, and thus the amplitude, of the standing wave component grows with the initial wave amplitude.

A standing wave component associated to the initial conditions (3.1) and (3.2) was also found by Hendrickson (2004) and Hendrickson & Yue (2006) where a careful analysis was carried out aimed at finding alternative initial conditions able to reduce their amplitude. It is worth noticing that the occurrence of the standing wave component is not affected by the horizontal size of the computational domain. The use of a computational domain of width equal to the fundamental wavelength λ only precludes wave components with longer wavelength to be described, whereas does

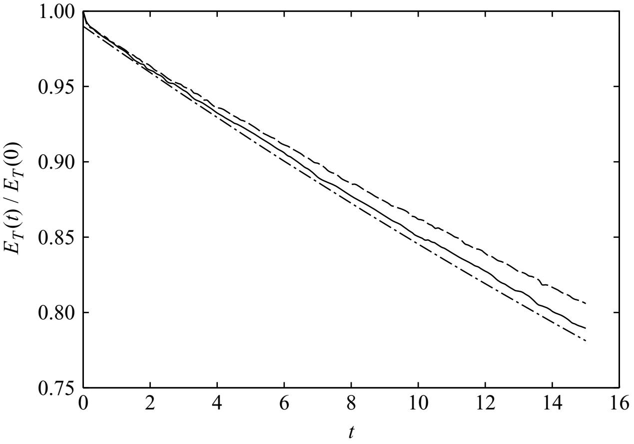

FIGURE 4. Time histories of the total mechanical wave energies for $\varepsilon = 0.2$ (solid) and $\varepsilon = 0.3$ (dash) non-dimensionalized by the corresponding initial values. The theoretical decay rate (dash-dot) is vertically shifted by a small amount to account for the initial drop in the energy profiles.

not significantly change the dynamics of the wave components of shorter wavelength. This statement has been verified in Iafrati (2006) where comparisons between results obtained for computational domains of width λ and 2λ have been established.

The purpose of the present work is to generate wave breaking flows of growing intensities and to investigate how the breaking intensity affects the transfer of momentum, the energy decay processes and the induced circulation. In this respect, the details of the mechanism inducing breaking are not expected to alter the gross features of the phenomena.

The time histories of the total energy for the two non-breaking cases are drawn in figure 4. At the very beginning, the curves exhibit a small drop which accounts for the energy transfer across the interface needed to accelerate the flow in air. Soon after the initial drop, the total energy decays smoothly and the numerical results are within the theoretical estimate $E_T(t) = E_T(0)\exp(-2\gamma t)$, where $\gamma = 2\mu_w/\rho_w k^2$ (Landau & Lifshitz 1959).

With the aim of evaluating to which extent the wave breaking enhances the dissipation, the time histories of the total wave energy are drawn in figure 5 for several values of the initial wave steepness. Results in figure 5(*a*, *c*) refer to the intermediate regime, which is from the non-breaking solution $\varepsilon = 0.3$ up to the plunging breaking case $\varepsilon = 0.4$ whereas in figure 5(*b*, *d*) results for all the plunging breaking cases, with steepness ranging from $\varepsilon = 0.4$ to 0.65, are shown. Figure 5(*a*) clearly indicates that the dissipation of the energy is significantly enhanced by the breaking process and that, at least in this intermediate regime, the energy fraction dissipated by the breaking grows very rapidly with the steepness, i.e. with the breaking intensity. In the plunging breaking regime, although the total amount of energy dissipated by the breaking does grow with the steepness, as seen from figure 5(*d*), the fraction of the initial wave energy dissipated by the breaking is almost independent of it. Similar results were also found experimentally by Rapp & Melville (1990).

Figure 5(*b*) indicates that, in the plunging breaking regime, a fraction between 44 % and 55 % of the initial energy content is dissipated by the breaking within two-wave periods after the breaking inception. It is worth noticing that the differences in the

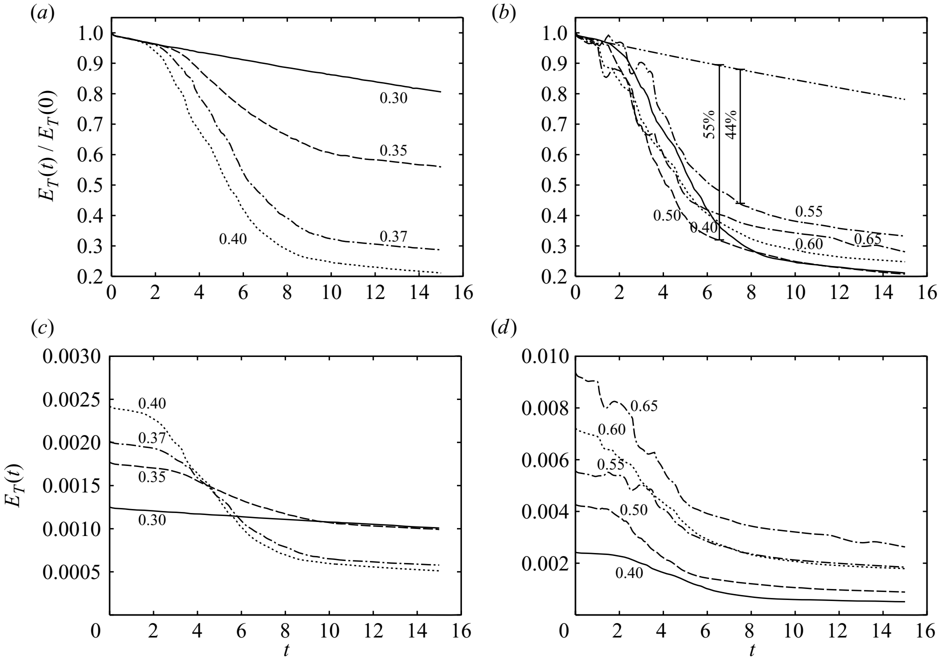

FIGURE 5. Effect of the breaking intensity on the total wave energy decay. In (*a*) and (*b*) the energy is divided by the corresponding initial value. In (*a*) and (*c*) the energy is drawn for $\varepsilon = 0.30$ (solid), 0.35 (dash), 0.37 (dash-dot) and $\varepsilon = 0.40$ (dot). In (*b*) and (*d*) for $\varepsilon = 0.40$ (solid), 0.50 (dash), 0.55 (dash-dot), 0.60 (dot) and 0.65 (dash-dash-dot). In (*b*) the theoretical estimate of the energy decay is also drawn (dot-dot-dash) in order to distinguish the energy fraction dissipated by the breaking.

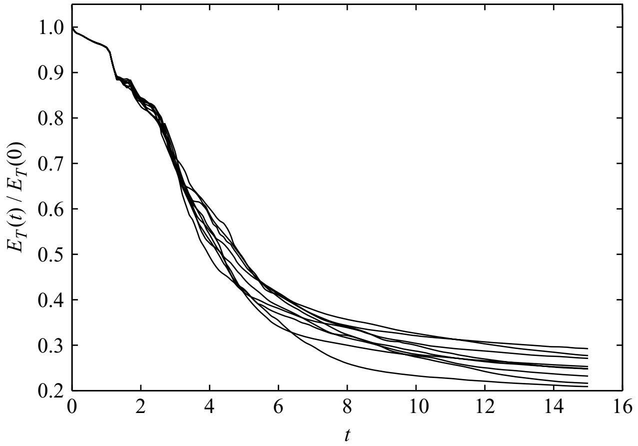

FIGURE 6. Time history of the non-dimensional energy obtained for $\varepsilon = 0.6$ and several values of the coefficient r in the initial conditions (3.3) and (3.4).

curves are not really related to the steepness but rather to the details of the breaking process. This is further supported by the fact that the differences found in terms of energy at the end of the simulations for different wave steepness are within the uncertainty of the single numerical simulation, as it can be seen from figure 6. In the

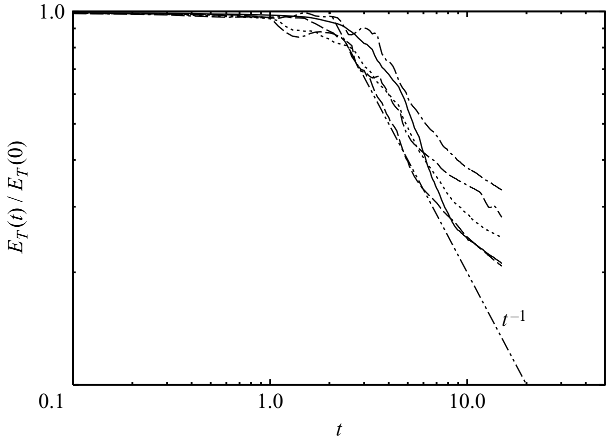

FIGURE 7. Time histories of the total mechanical wave energies in a log–log diagram. Curves are drawn for $\varepsilon = 0.4$ (solid), $\varepsilon = 0.5$ (dash), $\varepsilon = 0.55$ (dash-dot), $\varepsilon = 0.6$ (dot) and $\varepsilon = 0.65$ (dash-dash-dot-dot). The straight line is the t^{-1} decay rate.

figure the time histories of the energy obtained for $\varepsilon = 0.6$ and different shifts r in the initial conditions (3.3) and (3.4) are drawn.

In figure 7 the time histories of the total mechanical energy for the plunging breaking cases are drawn in a log–log diagram, along with a t^{-1} line. The figure shows that the energy follows the t^{-1} decay rate, at least during the most energetic phase of the breaking, whereas all curves approach a lower decay rate after $t \simeq 8$. A similar behaviour was found by Lubin *et al.* (2006).

In the experimental measurements done by Rapp & Melville (1990) and Melville *et al.* (2002), it was found that energetic breaking can dissipate as much as 40 % of the initial energy content and approximately 90 % of such amount is dissipated within four-wave periods after the breaking inception. Therein it was also shown that the kinetic energy of the flow and the total vorticity decay like t^{-1} afterwards. The numerical results discussed above display a general agreement with the experimental measurements by Rapp & Melville (1990) and Melville *et al.* (2002). Quantitatively, they exhibit a larger fraction of energy dissipated by the breaking and a lower decay rate of the energy in the very late stage. Although it is expected that the different methods adopted to generate breaking waves are partly responsible for the differences, a more careful analysis of the role played by the strongest assumption in the numerical simulations is needed.

The larger energy dissipation predicted by the numerical simulations cannot be ascribed to the two-dimensional assumption. Although the hypothesis is rather strong, it is not expected to change the solution significantly, at least in the early stage after the breaking inception. In fact, the overturning of the jet and first jet impact are basically two-dimensional processes. Three-dimensional effects are expected to matter only in the next stage when instabilities in the cross-direction strongly affect both the fragmentation process of the air cavity and the dynamics of the large vorticity structures. It is expected that smaller structures develop which, in a cascade, are rapidly dissipated under the action of the viscosity at the smallest scales. Owing to the enhanced dissipation caused by the turbulence, it is expected that three-dimensional effects, if included, would produce an even larger energy dissipation in comparison to the two-dimensional results. The above considerations are supported by the results presented in Lubin *et al.* (2006) where a comparison between the time histories of the energy obtained by two- and three-dimensional calculations is established. Therein it was shown that up to half-wave period after the breaking onset the energy curves are very close to each other whereas in a later stage the three-dimensional results exhibit a stronger dissipation. In the very late stage of the process, when the turbulent intensity is very low, aside from a different amount of energy left in water, there are no significant differences in terms of the energy decay rate.

It is worth remarking that three-dimensional effects are also important for the description of strong vorticity–free-surface interactions. In fact, the three-dimensional instabilities can generate striations on the free surface which eventually induce the three-dimensional fragmentation of the entrapped air bubbles (Sarpkaya & Suthon 1991). This has rather a relevant effect on the vorticity field and provides another mechanism for the entrainment of small air bubbles at the free-surface scars. A deeper investigation of the above phenomena is beyond the scope of the present work.

The second strong assumption concerns the low Reynolds number of the numerical simulations. In order to investigate this aspect it is useful to write the equation of the energy balance for a fluid with constant density and viscosity. From the momentum equation it follows that

$$\int_{\Omega} \rho \frac{\partial}{\partial t}\left(\frac{|\boldsymbol{u}|^2}{2}\right) \mathrm{d}V = \int_{\Omega} \rho u_i \left[-u_j \partial_j u_i - \frac{1}{\rho}\partial_i p + \frac{\mu}{\rho}\nabla^2 u_i\right] \mathrm{d}V - \int_{\Omega} \rho u_2 g \, \mathrm{d}V,$$

where, as explained earlier, the surface tension contribution has been neglected.

As the velocity field is divergence free, the first two contributions in the first integral can be recasted in the form of surface integrals whereas the second integral represents the time derivative of the potential energy. Thus the above equation becomes

$$\frac{\mathrm{d}E_T}{\mathrm{d}t} = -\int_{\partial\Omega} \rho \frac{|\boldsymbol{u}|^2}{2} \boldsymbol{u}\cdot\boldsymbol{n} \, \mathrm{d}S - \int_{\partial\Omega} p\boldsymbol{u}\cdot\boldsymbol{n} \, \mathrm{d}S + \int_V \mu \boldsymbol{u}\cdot\nabla^2 \boldsymbol{u} \mathrm{d}V,$$

where $\boldsymbol{n}$ is the unit normal vector outgoing from the water domain. By using again the zero divergence of the velocity field, it can be shown that

$$\boldsymbol{u}\cdot\nabla^2\boldsymbol{u} = \nabla\cdot[\boldsymbol{u}\times\boldsymbol{\omega}] - |\boldsymbol{\omega}|^2,$$

where $\boldsymbol{\omega}$ is the vorticity vector. Hence, the energy balance takes the form

$$\begin{aligned}\frac{\mathrm{d}E_T}{\mathrm{d}t} = & -\underbrace{\int_{\partial\Omega} \rho \frac{|\boldsymbol{u}|^2}{2} \boldsymbol{u}\cdot\boldsymbol{n} \, \mathrm{d}S}_{\text{kinetic energy flux}} - \underbrace{\int_{\partial\Omega} p\boldsymbol{u}\cdot\boldsymbol{n} \, \mathrm{d}S}_{\text{work by pressure}} + \underbrace{\int_{\partial\Omega} \mu(\boldsymbol{u}\times\boldsymbol{\omega})\cdot\boldsymbol{n} \, \mathrm{d}S}_{\text{work by tangential stresses}} \\ & - \underbrace{2\int_{\Omega} \mu \frac{|\boldsymbol{\omega}|^2}{2} \mathrm{d}V}_{\text{viscous dissipation}}, \end{aligned} \tag{3.6}$$

which clearly highlights the terms related to the energy flux through the air–water interface, the works done by pressure and tangential stresses at the interface and the viscous dissipation. Unfortunately, the use of a smooth density jump and of a finite region for the surface tension forces introduces a spurious velocity component within the transition region. Such spurious component, superimposed to the velocity field, makes the estimate of the surface integrals in (3.6) not reliable.

The most interesting aspect of (3.6) is that, aside from the contributions at the interface, it relates the dissipation in the field to the enstrophy, i.e. the integral over the fluid domain of the square of the vorticity amplitude. The vorticity level associated to the initial condition is low and it is concentrated in a very narrow region about the interface (Longuet-Higgins 1992). Moreover, due to the low density of the air the works done up to the breaking inception by pressure and tangential stresses at the interface are not very relevant. As a consequence, there is only a limited damping of the wave up to the time of breaking onset. This is clearly seen from figure 5(*b*) which shows that in all plunging cases the energy follows the theoretical decay rate before the breaking occurrence. In the early stage after the jet impact, two different phenomena occur which contribute to the dissipation of energy. The entrapment of the large air cavity generates a strong rotational flow in water. The diffusion of the vorticity makes the last term in (3.6) progressively larger. In addition to that, as discussed by Lamarre & Melville (1991) and more recently by Blenkinsopp & Chaplin (2007), there is significant amount of work to be done against buoyancy during the downward transport of the entrapped cavity. Whereas the viscous dissipation is expected to depend on the Reynolds number, the work done against the buoyancy is expected to be almost independent of it.

In order to further investigate this point, it is preferable to use a different form of the energy balance. In fact, although (3.6) is useful as it highlights the role played by the vorticity on the dissipation, a more common form of the energy balance equation is

$$\frac{\mathrm{d}E_T}{\mathrm{d}t} = \underbrace{-\int_{\partial\Omega} \rho \frac{|\boldsymbol{u}|^2}{2} \boldsymbol{u}\cdot\boldsymbol{n}\,\mathrm{d}S}_{\text{kinetic energy flux}} \underbrace{- \int_{\partial\Omega} p\boldsymbol{u}\cdot\boldsymbol{n}\,\mathrm{d}S}_{\text{work by pressure}} + \underbrace{\int_{\partial\Omega} u_i\sigma_{ij}n_j\,\mathrm{d}S}_{\text{work by viscous stresses}} - \underbrace{\int_{\Omega} \epsilon\,\mathrm{d}V}_{\text{viscous dissipation}}, \qquad (3.7)$$

where, for incompressible fluid, $\sigma_{ij} = 2\mu e_{ij}$ with e_{ij} denoting the symmetric part of the strain tensor. In (3.7)

$$\epsilon = 2\mu e_{ij}\frac{\partial u_i}{\partial x_j} \qquad (3.8)$$

is the local dissipation. Although in the case of unbounded flows or flows in closed domains with stationary boundaries it is

$$\int_{\Omega} \epsilon\,\mathrm{d}V = \int_{\Omega} \mu|\boldsymbol{\omega}|^2\,\mathrm{d}V, \qquad (3.9)$$

form (3.6) would give the wrong impression that the dissipation occurs in regions with high vorticity. This can be misleading as in regions of quasi-uniform vorticity there is an almost solid body rotation and hence no dissipation (Frisch 1995).

The viscous dissipation rate is evaluated as

$$K(t) = \int_{\rho=1} \epsilon\,\mathrm{d}V.$$

The above integral is evaluated in the pure water domain, i.e. the part of the computational domain where $\rho = 1$, so that the spurious velocity components generated by the artificial density variation do not affect the estimate. The time histories obtained for different steepnesses are drawn in figure 8 where the dissipation rate is divided by the corresponding initial energy content in water. The figure shows that, in the case $\varepsilon = 0.30$ the wavetrain remains regular and the dissipation rate

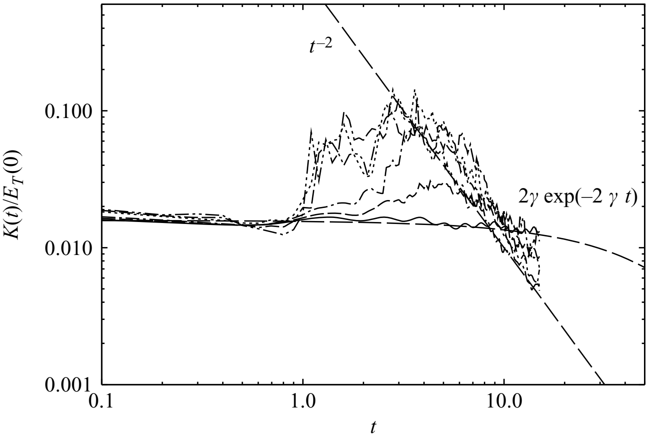

FIGURE 8. Time histories of the total dissipation in the pure water domain for different steepnesses: $\varepsilon = 0.30$ (solid), $\varepsilon = 0.35$ (dash), $\varepsilon = 0.40$ (dash-dot), $\varepsilon = 0.55$ (dot), $\varepsilon = 0.60$ (dash-dash-dot) and $\varepsilon = 0.65$ (dot-dot-dash). The theoretical curve for a regular wavetrain and the t^{-2} decay rate are drawn as well.

exhibits a small reduction with time, which is in close agreement with the theoretical estimate

$$\frac{1}{E_T(0)}\frac{\mathrm{d}E_T(t)}{\mathrm{d}t} = -2\gamma\exp(-2\gamma t)$$

discussed earlier. When wave breaking occurs, the dissipation grows sharply after the breaking onset. In the most energetic cases, it takes values about one order of magnitude larger than those found in the non-breaking regime and such high dissipation lasts for about one fundamental wave period. Next, the dissipation approaches a t^{-2} decay rate, which is consistent with the t^{-1} decay rate of the energy experimentally found.

It is worth recalling that the term analysed so far does not consider the contributions to the energy balance of the energy transfer in air and of the work done by pressure and viscous stresses at the interface. The results shown on figure 8 indicate that in all plunging breaking cases the viscous dissipation rate scaled by the initial energy content takes values around 0.06, between $t = 1$ and 3.5, i.e. about one-wave period after the breaking onset. Thus, in that interval, the viscous term can be at most responsible for the dissipation of 15 % of the initial energy content. This value is much less than the energy actually lost in all plunging breaking cases at $t = 3.5$, as it can be seen from figure 5(*b*). The additional amount of energy dissipated accounts for the contributions of the surface integrals in the energy balance and for the work done in entrapping the air cavity in particular. As aforesaid, the difficulties of the present model in providing reliable estimates of the surface integrals do not allow a more detailed investigation of such an important point.

In figure 9 the ϵ-contours are drawn for the same configurations as of figure 2(d, e, f) with the aim of showing the regions where the dissipation is localized. Countours are only drawn in the pure water domain, which is the region where $\rho = 1$, thus avoiding the misleading effect of the spurious velocity components occurring inside the transition region. The figures indicate that the dissipation is mainly localized in a narrow region about the interface, with the strongest values taking place nearby the small air bubbles generated by the collapse of the air cavity entrapped by the

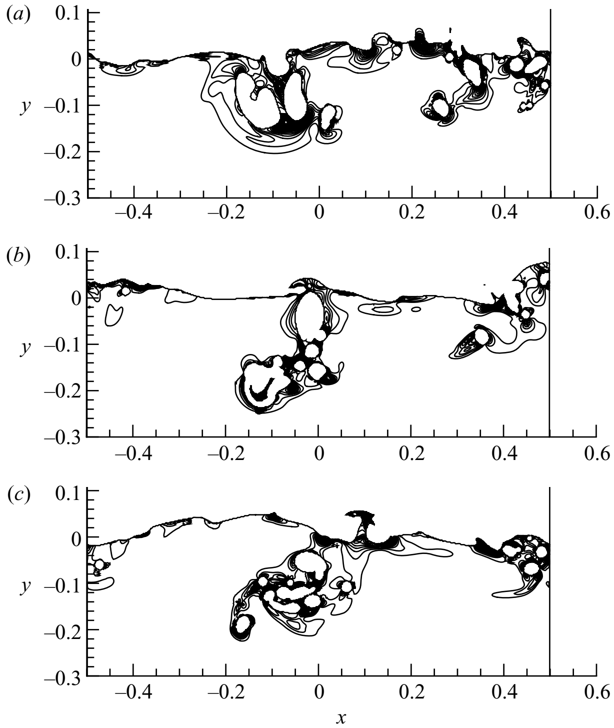

FIGURE 9. From top to bottom, dissipation contours at $t=4.0, 4.6$ and 5.2 for $\varepsilon=0.60$. Isocurve step is $\Delta\epsilon=0.002$.

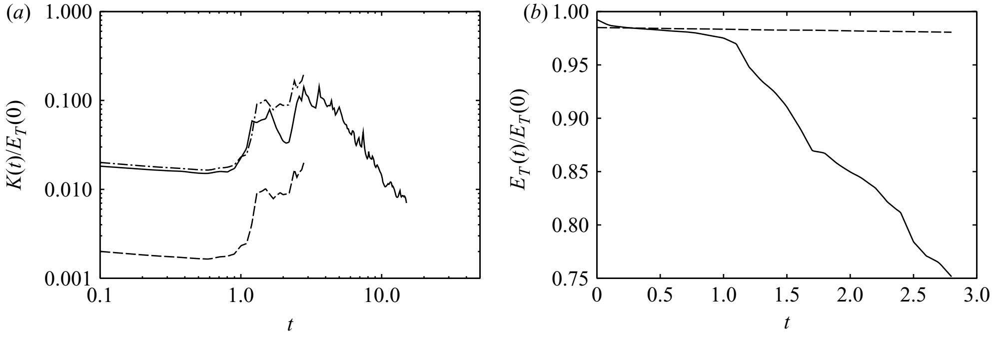

FIGURE 10. Time histories of the viscous dissipation rates at different Reynolds number (*a*) and of the total energy for the simulation at $Re=10^5$ (*b*). In both cases results are scaled by the initial energy content in water. In (*a*) the solid and dashed lines refer to the simulation at $Re=10^4$ and 10^5, respectively. The dash-dotted line is the viscous dissipation rate found at $Re=10^5$ multiplied by a factor 10. In (*b*) the dashed line represents the theoretical decay rate for non-breaking waves $Re=10^5$.

plunging jet. Sharp velocity gradients are induced by the interaction of the rotating structures with the surrounding fluid at rest.

In order to evaluate the role played by the Reynolds number on the energy fraction dissipated by the breaking, the numerical simulation for $\varepsilon=0.55$ is repeated by using $Re=10^5$. In figure 10(*a*) the time history of the viscous dissipation rate calculated for $Re=10^5$ is compared with that found at $Re=10^4$. The curve for the two Reynolds number are essentially parallel to each other up to $t \simeq 1.3$. This is even clearer if the curve obtained for $Re = 10^5$ is multiplied by a factor 10 to account for the different viscosity in the two simulations. The fact that the two curves of the viscous dissipation scale with the viscosity indicates that the flow fields in the two cases are essentially the same, at least up to $t = 1.3$, and, as expected, the viscous dissipation rate is much smaller at the higher Reynolds number.

Between $t = 1$ and 2.8, which is about 0.7 wave periods $Re = 10^5$, the average value of the viscous dissipation is 0.01. Hence, in that time interval, this effect can be responsible for the dissipation of only 2 % of the initial energy content. This value is remarkably less than the amount of total energy lost in the same interval, which is about one-fourth the initial energy content, as it can be seen from figure 10(*b*). Again, this result confirms that viscous dissipation does not significantly contribute to the energy decay, at least up to about one-wave period after the breaking onset.

In figure 10(*b*) the time history of the total energy for $Re = 10^5$ is compared with the theoretical decay rate discussed earlier. As already explained, the sudden drop of the energy is caused by the work done in accelerating the air phase, which is at rest at the beginning. In the next stage, up to the breaking onset at $t \simeq 1$, the decay rate of the numerical solution is a little higher than the theoretical estimate. Although the difference is less than 1 % at the onset of breaking, the larger dissipation indicates that the grid resolution adopted is not sufficient yet to resolve the smallest scales and the numerical scheme introduces some artificial dissipation.

As aforementioned, comparisons with results obtained with a coarser grid, not shown here, indicate that a satisfactory agreement is achieved in terms of global quantities. In this sense, although the grid discretization is not enough to resolve the finest details of the flow, the scales that mainly govern energy and the circulation seem correctly captured, at least up to half-wave period after the breaking onset. In a later stage of the process, it is expected that much smaller scales develop which are expected to influence the dissipation of energy, thus deserving a more accurate description. At such stage, however, also the three-dimensional effects must be accounted for.

Figure 10(*a*) indicates that for $t > 1.3$, the scaled dissipation for $Re = 10^5$ is larger than the viscous dissipation found at $Re = 10^4$. On the other hand, as shown in figure 27, the total amount of circulation in water at the two different Reynolds numbers is about the same. According to (3.9), a larger viscous dissipation in presence of a comparable circulation can be explained with smaller structures developing at higher Reynolds number. The occurrence of smaller structures at the higher Reynolds number is confirmed by the free-surface profiles drawn in figure 11. Profiles are rather similar but the solution at $Re = 10^5$ exhibits smaller bubbles and drops already at $t = 1.8$.

3.4. *Vertical transfer of horizontal momentum*

With the aim of analysing the vertical transfer of the horizontal momentum, the flux

$$f(y, t) = \int_{-0.5}^{0.5} \rho u v \, \mathrm{d}x \tag{3.10}$$

is evaluated throughout the simulation along several horizontal planes, from $y \simeq 0$ to $y \simeq -0.375$, with a vertical spacing of 0.025 among them. In order to avoid interpolation of the velocity field, the y-coordinate of the planes is assumed equal to that of the closest cell centres row. The total amount of horizontal momentum

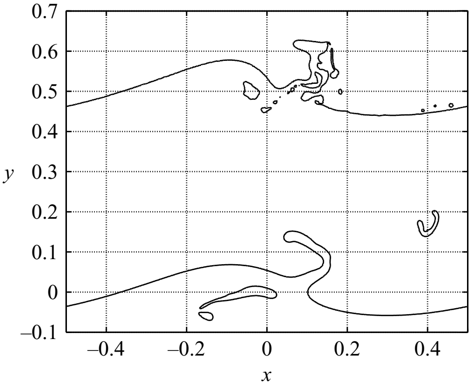

FIGURE 11. Free-surface profiles obtained for an initial wave steepness $\varepsilon = 0.55$ at $t = 1.8$ at $Re = 10^4$ (bottom) and $Re = 10^5$ (top). A vertical shift of 0.5 is applied to the profile obtained at $Re = 10^5$ to make the comparison easier.

transferred at a given time t across the y-planes is calculated as

$$q(y,t) = \int_0^t f(y,\tau)\,\mathrm{d}\tau, \tag{3.11}$$

and the corresponding time histories across several planes and for different steepness are drawn in figure 12.

The figures show that in the most energetic plunging breaking cases the integral of the horizontal momentum flux across the planes is averagely negative, at least for the planes with $y > -0.2$, which is consistent with a net downward transfer of the horizontal momentum from the upper layers towards the bulk of the fluid beneath. The comparison among the curves for the same steepness ε at different planes highlights a delay in the transfer process, with the higher planes being involved earlier than the lower ones, and a progressive diminishing of the amplitude of the flux going deeper. The difference in the amount of momentum transferred across two successive planes represents the portion of horizontal momentum that remains between the two planes in the form of horizontal current. At least for the case $\varepsilon = 0.6$, and for the planes lying below $y \simeq -0.2$, the integral of the horizontal momentum flux becomes positive in the later stage of the simulation. As it is shown later on, this is due to the presence of the strong clockwise-rotating structure formed by the breaking process.

A better comprehension of the momentum transfer operated by the breaking can be inferred from figure 13 where the vertical profiles of $q(y,t)$ are drawn at $t = 10$ and 15. The figures show that, generally speaking, for $y > -0.15$ the total flux of horizontal momentum grows in amplitude with the breaking intensity and that the stronger is the breaking intensity the thicker is the surface layer affected by the vertical transfer of momentum. Figure 13(*b*) also indicates that for $\varepsilon \geqslant 0.55$ a change in the sign of $q(y,t)$ occurs for $y \simeq -0.15$. The downward transfer occurring across the upper layer is consistent with the presence of a shear flow whereas the change in the sign, and thus an upward transfer of the horizontal momentum, indicates the presence of clockwise-rotating vortex structures generated at the breaking onset when the large air cavity is entrapped (see figure 2). The occurrence of a clockwise-rotating vortex structure slowly drifting downstream was also experimentally found by Melville *et al.* (2002) and numerically studied by Sullivan *et al.* (2004).

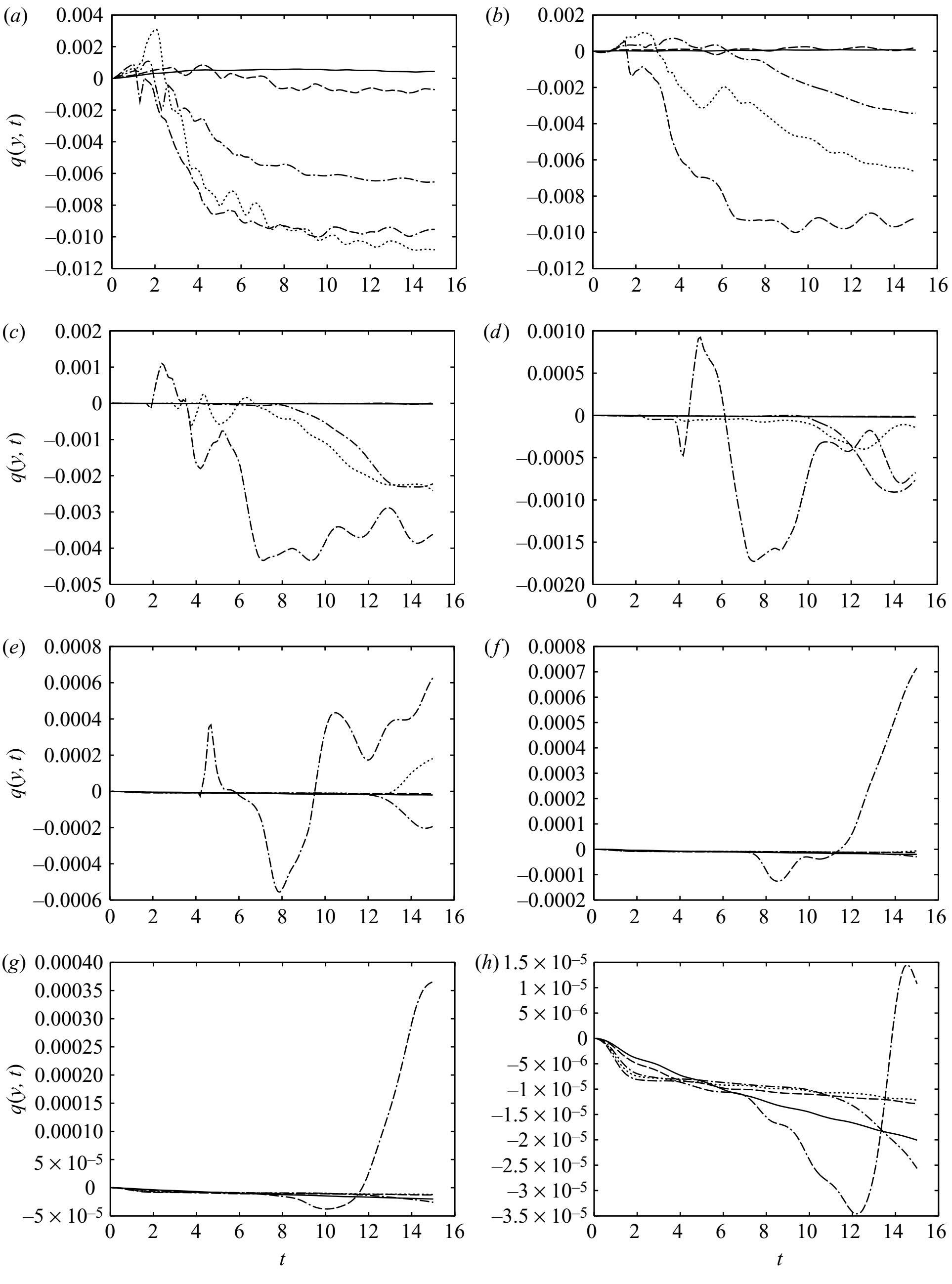

FIGURE 12. Time histories of the total flux of horizontal momentum across several horizontal planes: (*a*) $y \simeq -9.765\ 10^{-4}$; (*b*) $y \simeq -5.176\ 10^{-2}$; (*c*) $y \simeq -0.1006$; (*d*) $y \simeq -0.1517$; (*e*) $y \simeq -0.2002$; (*f*) $y \simeq -0.2510$; (*g*) $y \simeq -0.3018$; (*h*) $y \simeq -0.3506$. Results are drawn for $\varepsilon = 0.35$ (solid), $\varepsilon = 0.40$ (dash), $\varepsilon = 0.50$ (dash-dot), $\varepsilon = 0.55$ (dot) and $\varepsilon = 0.60$ (dash-dash-dot).

By introducing the horizontal average of an arbitrary function $g(x, y, t)$ as

$$\langle g\rangle(y, t) = \int_{-0.5}^{0.5} g(x, y, t)\,\mathrm{d}x, \tag{3.12}$$

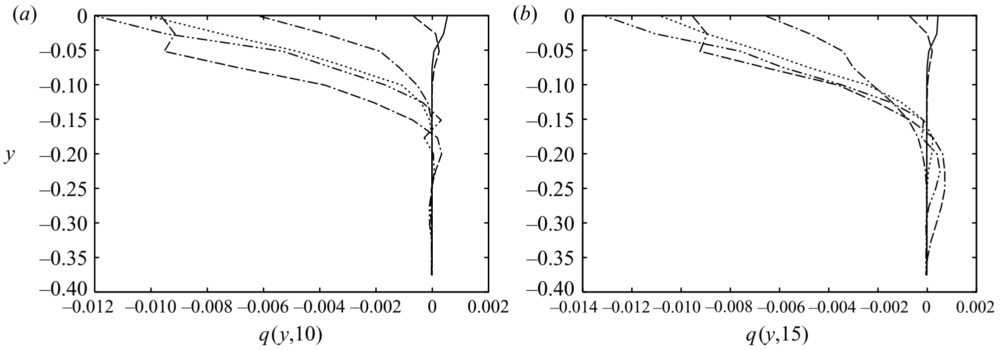

FIGURE 13. Vertical profiles of the total flux of horizontal momentum taken at $t = 10$ (*a*) and $t = 15$ (*b*). Results are drawn for $\varepsilon = 0.35$ (solid), $\varepsilon = 0.40$ (dash), $\varepsilon = 0.50$ (dash-dot), $\varepsilon = 0.55$ (dot), $\varepsilon = 0.60$ (dash-dash-dot) and $\varepsilon = 0.65$ (dot-dot-dash).

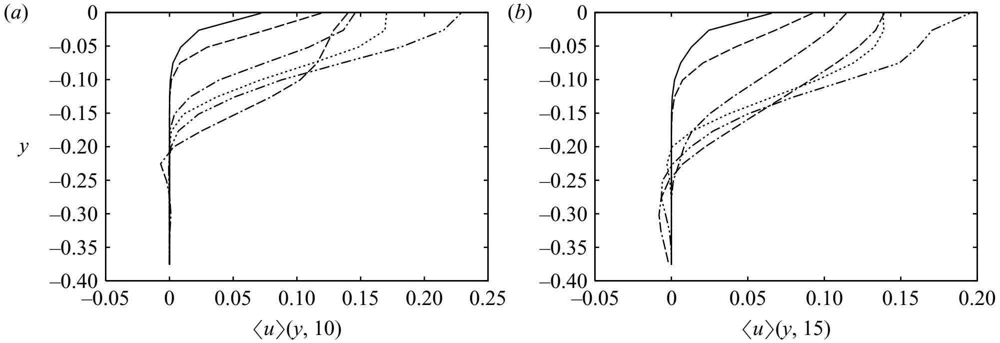

FIGURE 14. Vertical profiles of the average horizontal velocity $t = 10$ (*a*) and $t = 15$ (*b*). Results are drawn for $\varepsilon = 0.35$ (solid), $\varepsilon = 0.40$ (dash), $\varepsilon = 0.50$ (dash-dot), $\varepsilon = 0.55$ (dot), $\varepsilon = 0.60$ (dash-dash-dot) and $\varepsilon = 0.65$ (dot-dot-dash).

the shear layer and the presence of large vortex structures can be recognized from the vertical profiles of the horizontal average of the horizontal velocity component $\langle u\rangle(y, t)$ which are drawn in figure 14 for different steepnesses and two time instants. It is worth remarking that, since the present analysis is mainly focused on the early stage after the breaking onset, the current induced by the breaking is still growing in amplitude. On the basis of the analysis done by Rapp & Melville (1990), this current should decay in amplitude with time afterwards, although very slowly.

Figures 13 and 14 show that for $\varepsilon = 0.65$ surface layer affected by the momentum transfer is shallower than the one found for $\varepsilon = 0.6$, although the surface current is stronger. This can be explained by looking at the vertical profiles of the horizontal average of the density $\langle \rho\rangle(y, t)$ that are given in figure 15 for $\varepsilon = 0.55, 0.60$ and 0.65 at $t = 10$ and 13. The figures clearly indicate that for $\varepsilon = 0.65$ a much larger amount of air is entrained compared to weaker breaking cases and, moreover, air bubbles are convected deeper. As a consequence of the lower density value, in spite of the larger velocities, a reduced amount of horizontal momentum is transferred to the bulk of the fluid beneath at a given level and at the same time instant. At $t = 15$ all the entrapped air bubbles have left the water and below the still water level the density is essentially constant for all cases.

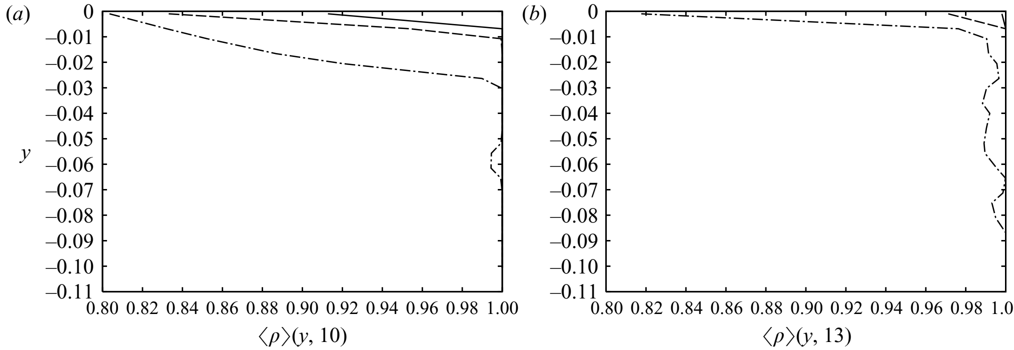

FIGURE 15. Vertical profiles of the horizontal averaged density $t = 10$ (*a*) and $t = 13$ (*b*). Results are drawn for $\varepsilon = 0.55$ (solid), $\varepsilon = 0.60$ (dash) and $\varepsilon = 0.65$ (dash-dot).

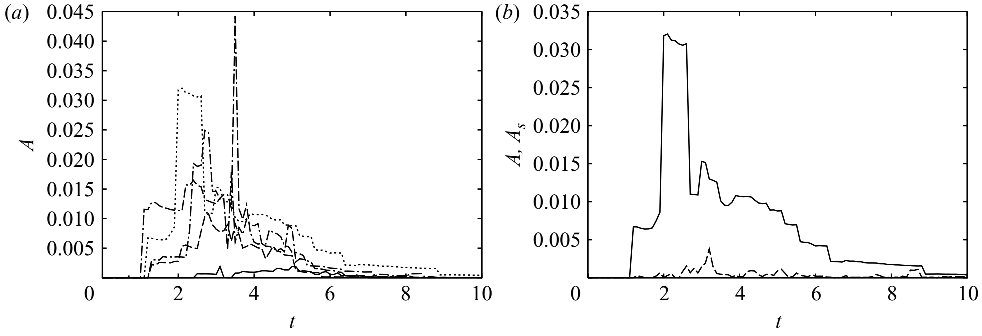

FIGURE 16. In (*a*) the time histories of the total area of air entrained by the breaking of waves of different steepnesses are drawn for the cases $\varepsilon = 0.40$ (solid), $\varepsilon = 0.50$ (dash), $\varepsilon = 0.55$ (dash-dot), $\varepsilon = 0.60$ (dot) and $\varepsilon = 0.65$ (dash-dash-dot). In (*b*) the total area of air entrained in the case $\varepsilon = 0.60$ (solid) is drawn along with the corresponding area of the unresolved bubbles A_s (dash).

The above findings suggest that, if the waves are steep enough, the surface layer affected by the breaking could actually be narrower for larger amplitudes due to the role played by the air entrainment. Such important aspects have to be taken into account in developing and using numerical models for the oceanic boundary layer like that developed in Sullivan *et al.* (2004). In that model the occurrence of breaking is modelled as a forcing term into the governing equations. It is believed that the above considerations about the role played by the bubbles on the vertical transfer of momentum are of help for the definition of the forcing term of the breaker model. This is particularly true for those cases when large air entrainment occurs and the resulting effects in terms of buoyancy and momentum have to be properly described.

3.5. *Air entrainment and degassing process*

The detailed set of data provided by the numerical simulations allows a quantitative analysis of the air entrainment and of the degassing process. In figure 16(*a*) the time histories of the total area of air entrained by the breaking event at different steepnesses are drawn. The curves clearly show the entrapment of the large air cavity at the breaking onset. After a time interval during which the area remains constant, the time histories evidence a sharp rise and a subsequent drop. The sharp rise and drop of the area are related to the plunging of the splash up jet. As the filament of

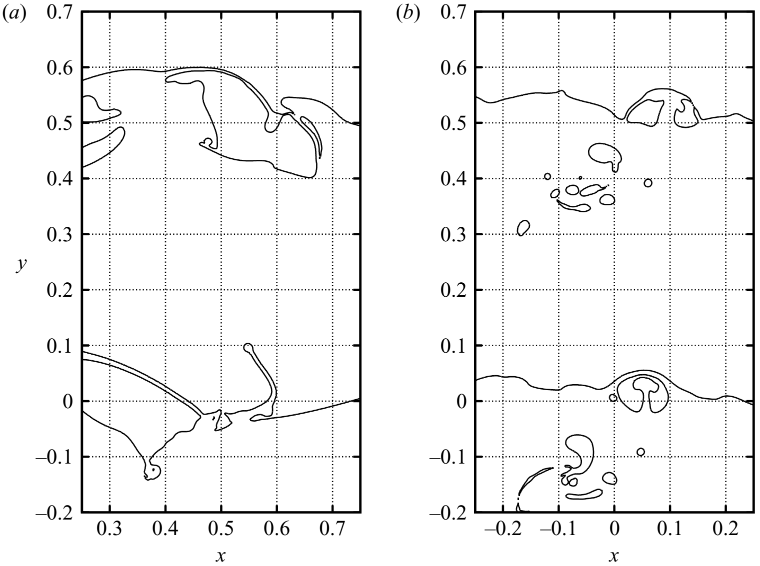

FIGURE 17. In (*a*) the free-surface profiles at $t = 2.0$ and 2.7 for $\varepsilon = 0.60$ are compared to show the entrapment and the subsequent release of a large air cavity operated by the splash-up jet. In (*b*) the free-surface profiles for the same simulation at $t = 5.0$ and 5.2 are compared to show the vertical rise of the air bubbles towards the free surface. In both cases a vertical shift of 0.5 is applied between the two profiles to make the comparison easier.

water that encompasses the cavity is rather thin, it rapidly collapses, letting the air in the cavity to escape. The above phenomenon can be easily recognized by comparing the time history of the entrapped air for $\varepsilon = 0.6$, drawn in figure 16(*b*), with the free-surface profiles at $t = 2.0$ and 2.7 displayed by figure 17(*a*).

Figure 16(*a*) indicates that, in a later stage, the amount of air entrapped decays with time. From the free-surface profiles given in figure 17(*b*) it can be seen that bubbles gradually rise back towards the free surface and eventually escape from the water. The above is the primary mechanism for the degassing of the air bubbles. However, before drawing any quantitative estimate of the degassing process, it is important to analyse the limits imposed by the adopted grid discretization in connection with the smallest bubbles.

As explained in § 2.2, the present numerical model cannot describe a closed contour if the thickness is smaller than one grid cell. Furthermore, due to the spreading of the density and viscosity jumps across a transition layer of thickness $2\delta_P$, bubbles or air filaments thinner than $2\delta_P$, cannot be considered fully resolved. In order to distinguish between resolved and unresolved bubbles, an average thickness is evaluated. For each bubble, the average thickness is defined as the ratio between the area of the bubble and the maximum between the horizontal and the vertical dimensions of the bubble. A bubble is considered unresolved when the average thickness falls below $2\delta_P$. In figure 16(*b*) the total area of the unresolved bubbles A_s is drawn together with the total area of the entrapped air A. The figure indicates that the area of the unresolved bubbles is very small compared to the total area up to about half-wave period after the breaking onset. Next, due to the fragmentation of the air cavity it grows and in the worst conditions it gets up to one-fourth of the total area.

The artificial degassing of thin air filaments or bubbles operated by the numerical scheme, can be quantitatively estimated from the total area occupied by water A_w,

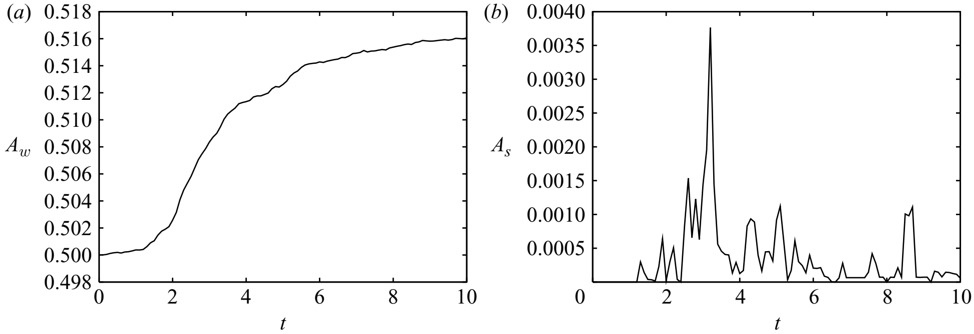

FIGURE 18. Time histories of the total area occupied by water A_w (*a*) and of the unresolved bubbles A_s (*b*) for the case $\varepsilon = 0.60$.

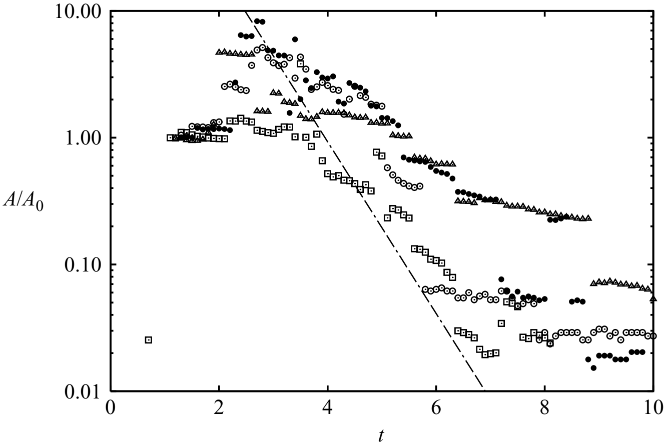

FIGURE 19. Time histories of the total area of the entrapped bubbles divided by the area of the air cavity generated at the breaking onset A_0. Results refer to $\varepsilon = 0.50$ (⊙), $\varepsilon = 0.55$ ●, $\varepsilon = 0.60$ (▲), $\varepsilon = 0.65$ (⊡). The line represents the exponential decay rate $C \exp(-3.9(t - t_b)/T)$, where $t_b = 1$, $T = 2.5$ and $C = 10^2$.

drawn in figure 18(*a*) for the case $\varepsilon = 0.60$. The comparison with the corresponding area of the unresolved bubbles given in figure 18(*b*) indicates that the sharpest increase in the water area occurs between $t = 2.0$ and 4.0, during which the total area of the unresolved bubbles take the largest values. In total, at the end of the numerical simulation, the artificial degassing can be estimated in about 3 % of initial water area.

With the aim of deriving a quantitative estimate of the degassing rate, the time histories of the total area occupied by air bubbles are scaled by the area A_0 of the air cavity entrapped at the breaking onset. Results, drawn in figure 19, are compared with the decay rate proposed by Lamarre & Melville (1991), who found that the scaled air volume behaves as $C \exp(-3.9(t - t_b)/T)$, where t_b is the time of breaking onset and T is the wave period. In Lamarre & Melville (1991) the constant $C = 2.6$ accounts for the initial period, duration of which is approximately $T/4$, during which the amount of air entrapped remains nearly constant. In the comparison established below it is assumed $t_b = 1$ and $T = 2.5$ whereas a different value of the constant $C = 10^2$ is needed to get a better agreement.

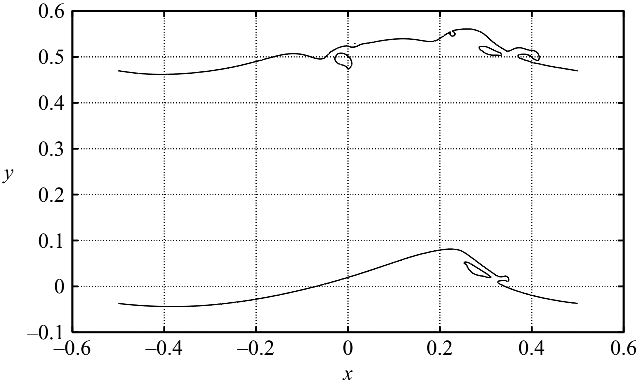

FIGURE 20. Free-surface profiles at $t = 2.6$ and 4.8 for $\varepsilon = 0.40$. A vertical shift of 0.5 is applied to the profile at $t = 4.8$. Due to the standing wave component, a second plunging event takes place about one-wave period after the breaking onset.

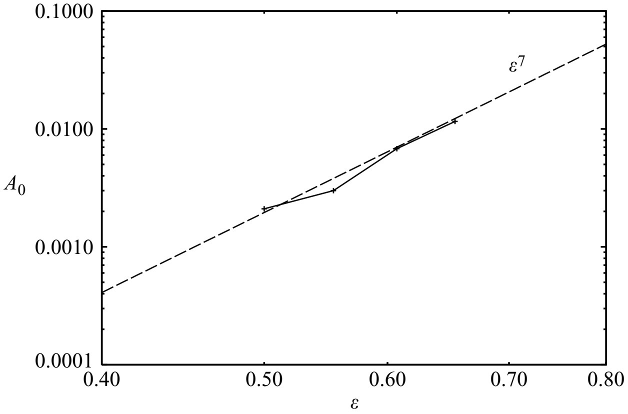

FIGURE 21. Area of the air cavity entrapped at the breaking onset versus the steepness.

The need of a different constant stems from the longer interval of time during which the amount of air remains constant in the present simulations. The reason for that has to be ascribed to the standing wave component. This can be easily seen from the sequence given in figure 1(*d*) and more clearly from the free-surface profiles drawn in figure 20. Due to the standing wave, a second plunging event and a new splash up occur about one-wave period after the breaking onset. Although this second event is milder because an important amount of energy has already been lost by the wave, it leads to the entrapment of new air cavities.

Aside from the different constant, the comparison shown in figure 19 indicates that the curves follow the exponential decay in the early stage. In a later stage, probably because of the difficulties of the numerical model in achieving a complete description of the fragmentation process, numerical results display a lower decay rate.

In order to achieve a quantitative estimate of the effects of the breaking intensity on the amount of air entrapped, in figure 21 the area of the air cavity entrapped at the onset of the stronger breaking cases versus the steepness is drawn. The data indicate that, for the range of steepnesses considered here, the area of the air cavity

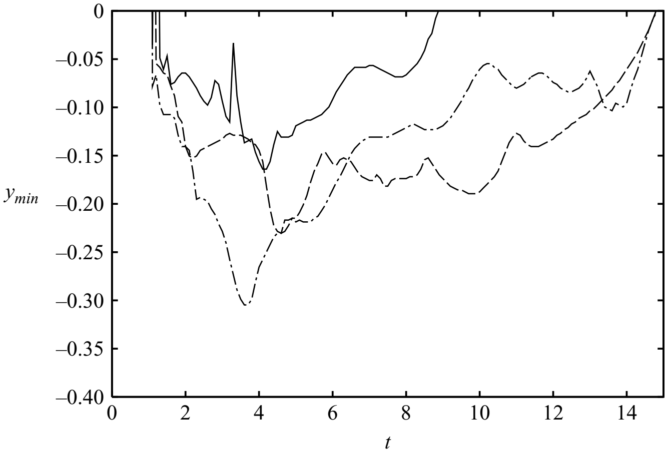

FIGURE 22. Time histories of the minimum y-coordinate of the bubbles. Results refer to $\varepsilon = 0.55$ (solid), $\varepsilon = 0.60$ (dash) and $\varepsilon = 0.65$ (dash-dot).

entrapped by the first breaking event grows as ε^7. At present it is not possible to estimate to which extent such relation depends on the initial conditions adopted here.

As discussed in the previous section, the downward transfer of momentum depends not only on the amount of air entrapped, but also on the depth of the bubbles. In figure 22, the time history of the minimum y-coordinate of the air bubbles is drawn for the three stronger breaking cases. The curves indicate that stronger breaking event pushes the air much deeper. This is due to the combined effects of the larger cavity entrapped at the first plunging event, i.e. a larger rotating structure, and of the stronger velocity. Bubbles remain at the minimum y-coordinate only for a short time as they are pushed back towards the free surface by both the buoyancy and the upward velocity induced by the clockwise-rotating structure.

3.6. *Rotational flow induced in water*

As seen before, the occurrence of breaking generates a strong rotational flow in water. Depending on the breaking intensity, vorticity can be generated by either viscous effects, as it happens in the spilling breaking type, or inviscid mechanisms, like the reconnection process in the plunging breaking type. In the latter case, as shown in figure 2 (d, e, f), in addition to the primary circulation generated by the topological change, strong secondary vorticity structures, of opposite sign, may appear as a result of the viscous interaction of the primary structures with the surrounding fluid at rest.

On the basis of the above considerations, a better understanding of the vorticity field induced by the breaking process can be achieved distinguishing between positive and negative values. To this aim, the circulations associated to the positive and negative vorticities, denoted by Γ_P and Γ_N, respectively, are defined as

$$\Gamma_P = \int_{\rho=1} \max(0, \omega)\, \mathrm{d}V \quad \Gamma_N = \int_{\rho=1} \min(0, \omega)\, \mathrm{d}V. \tag{3.13}$$

Integration is carried out over the pure water domain in order to avoid any misleading effect induced by the spurious velocity component taking place within the transition region. The time histories of the circulations associated to the positive and negative

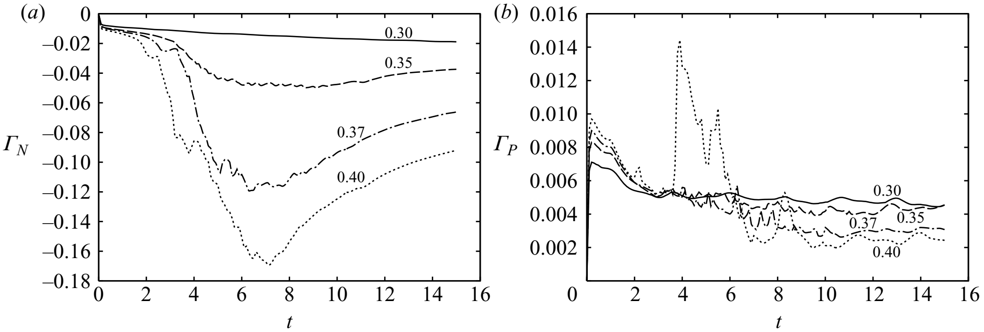

FIGURE 23. Time histories of the negative (a) and positive (b) circulations in the water domain obtained for several initial wave steepnesses: $\varepsilon = 0.30$ (solid), $\varepsilon = 0.35$ (dash), $\varepsilon = 0.37$ (dash-dot) and $\varepsilon = 0.40$ (dot). In this range of variation of the initial wave steepness, the resulting wave flow changes from regular to the plunging breaking regime.

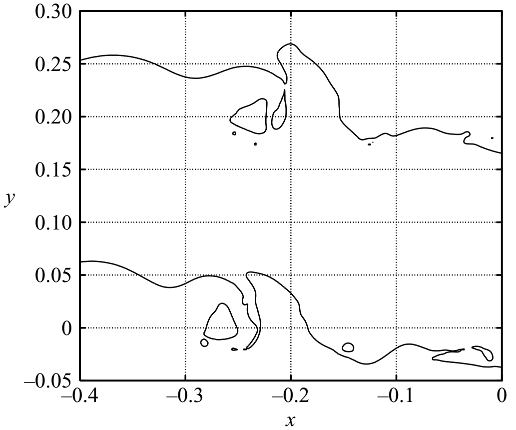

FIGURE 24. Free-surface profiles for $\varepsilon = 0.40$ at $t = 3.6$ (bottom) and 3.7 (top). A vertical displacement of 0.2 is applied to the profile at $t = 3.7$.

vorticity for the different values of the initial wave steepness are drawn in figures 23 and 25.

In figure 23 curves refer to wave steepnesses ranging from $\varepsilon = 0.30$ to 0.40, i.e. the intermediate region where the final wave system changes from regular to spilling and plunging breaking regimes. According to this change in the flow, a significant variation of the negative circulation generated in water occurs. The comparison among the time histories of Γ_N, drawn in figure 23(a), shows that the transition from the spilling to the plunging breaking regime, taking place between $\varepsilon = 0.35$ and 0.37, causes a sharp increase in the amount of negative vorticity generated in water. This clearly indicates that the free-surface reconnection that characterizes plunging breaking events is a very efficient mechanism for vorticity production. The positive circulation, shown in figure 23(b), exhibits a more irregular behaviour and is much lower than the negative one. For ε up to 0.37, there are no significant changes among the different steepnesses. Different considerations deserve the case with $\varepsilon = 0.40$, in which a sharp growth in the positive vorticity occurs about $t = 3.7$. Such a rapid increase in the circulation is again related to a reconnection process at the free surface as it can be seen from figure 24 where the free-surface profiles at $t = 3.6$ and 3.7 are drawn. The solution at $t = 3.6$

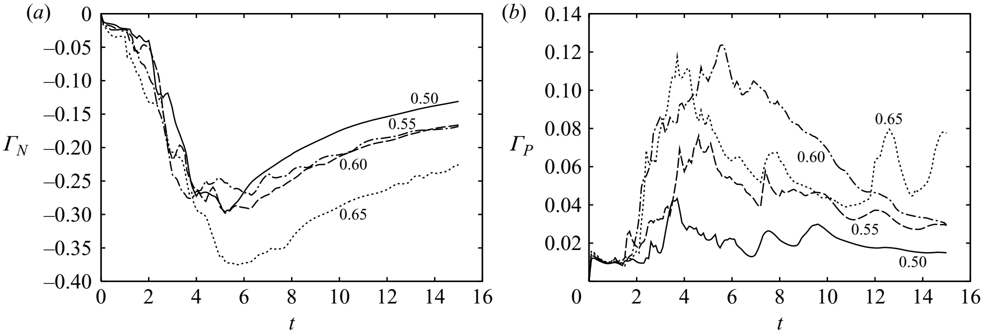

FIGURE 25. Time histories of the negative (*a*) and positive (*b*) circulations in the water domain obtained for several initial wave steepnesses in the plunging breaking regime: $\varepsilon = 0.50$ (solid), $\varepsilon = 0.55$ (dash), $\varepsilon = 0.60$ (dash-dot) and $\varepsilon = 0.65$ (dot).

shows the air cavity generated by the first plunging event. The rotating structure leads to the formation of a cusp on the free-surface profile. The clockwise-rotating flow makes the cusp deeper and beyond a certain limit, the free surface on the right of the cusp plunges on the free surface on the left and leads to the cavity closure. Such reconnection process is responsible for the generation of the positive circulation around the cavity taking place about $t = 3.7$ in figure 23(*b*). However, owing to the smaller size of the cavity and to the lower velocity of the backward propagating front that causes the free-surface reconnection, the positive circulation generated by that process is about an order of magnitude smaller than that generated by the first plunging event.

In order to analyse the changes induced by the breaking intensity, the time histories of the circulations found in the plunging breaking regime are drawn in figure 25. For $\varepsilon \geqslant 0.5$, curves of Γ_N are very close to each other in the early stage after the breaking onset, aside from the case $\varepsilon = 0.65$ in which the maximum of negative circulation takes a much larger value. Differently from the negative contribution, the total amount of positive vorticity displays a general growth with the initial steepness not always monotonic, though. Relatively speaking, the maximum amplitude of the positive circulation is much larger than that found in the intermediate regime. For the highest steepnesses, the peak value is as large as 40 % of the corresponding peak of the negative circulation.

The above analysis does not account for the different breaking intensity. With the aim of achieving a fairer comparison, the circulation associated to the negative vorticity is divided by the velocity jump $(u_c - u_t)$ between the velocity at the crest u_c and the velocity at the trough u_t. The corresponding time histories are drawn in figure 26. Such a scaling makes even clearer the increase in the vorticity production occurring as the breaking changes from spilling to plunging. Furthermore, results indicate that in the most energetic phase of the breaking in all the plunging cases, i.e. $\varepsilon \geqslant 0.37$, the ratio is within 0.3 and 0.5, independent of the initial wave steepness.

Finally, in order to evaluate the effect of the Reynolds number on the circulations, results found at the two Reynolds number for the case $\varepsilon = 0.55$ are drawn in figure 27. Also in terms of positive and negative circulations, the Reynolds number does not seem to play a relevant role, at least up to about $t = 2.5$, i.e. about half-wave period after the breaking onset.

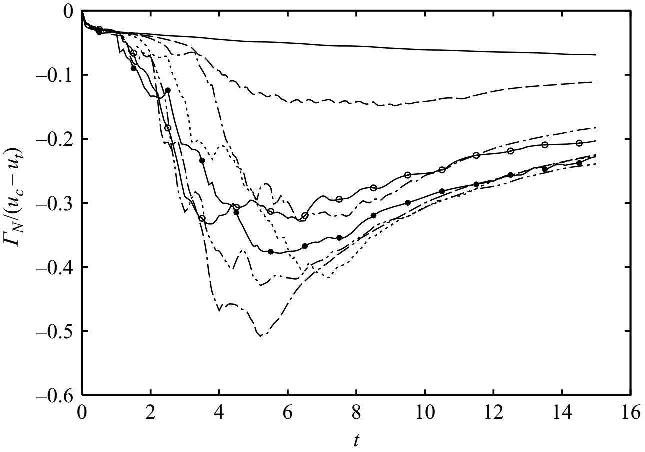

FIGURE 26. Time histories of the circulation associated to the negative vorticity field for different initial wave steepnesses. In the graph, curves are scaled by the velocity jump between the crest and the trough of the wavetrain: $\varepsilon = 0.30$ (solid), $\varepsilon = 0.35$ (dash), $\varepsilon = 0.37$ (dash-dot), $\varepsilon = 0.40$ (dot), $\varepsilon = 0.50$ (dash-dash-dot), $\varepsilon = 0.55$ (dot-dot-dash), $\varepsilon = 0.60$ (solid-○) and $\varepsilon = 0.65$ (solid-●).

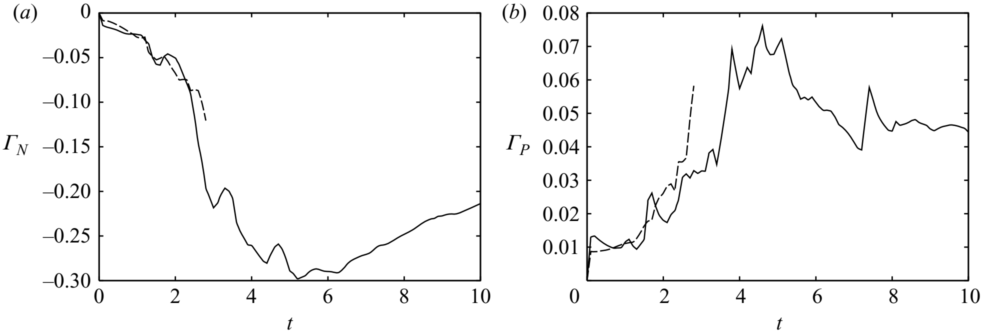

FIGURE 27. Time histories of the circulation associated to the negative (*a*) and positive (*b*) vorticities obtained for $\varepsilon = 0.55$ at $Re = 10^4$ (solid) and $Re = 10^5$ (dash).

3.7. *Uncertainty of the results and intermittency*

Results presented above are obtained with single numerical simulations of the time evolution of wavetrains of different initial steepness. Owing to the strong nonlinearity of the flow, it is important to estimate to which extent solutions are affected by small perturbations in the initial conditions. In the experiments, it is a usual practice to perform several repetitions of the test and to establish an ensemble average among the measurements. The residual motions of the free surface and of the fluid are strong enough to introduce measurable changes. In the numerical case, the perturbation has to be explicitly introduced otherwise no differences can be found.

Here, the numerical simulation for the case with $\varepsilon = 0.60$ is repeated 10 times using different values of the parameter r in the initial conditions (3.3) and (3.4). The phase shift in the initial conditions, although smaller than the grid spacing, causes relevant changes to the dynamics of the breaking event and thus to the size and the distribution of the air bubbles. In order to quantify these differences, an intermittency

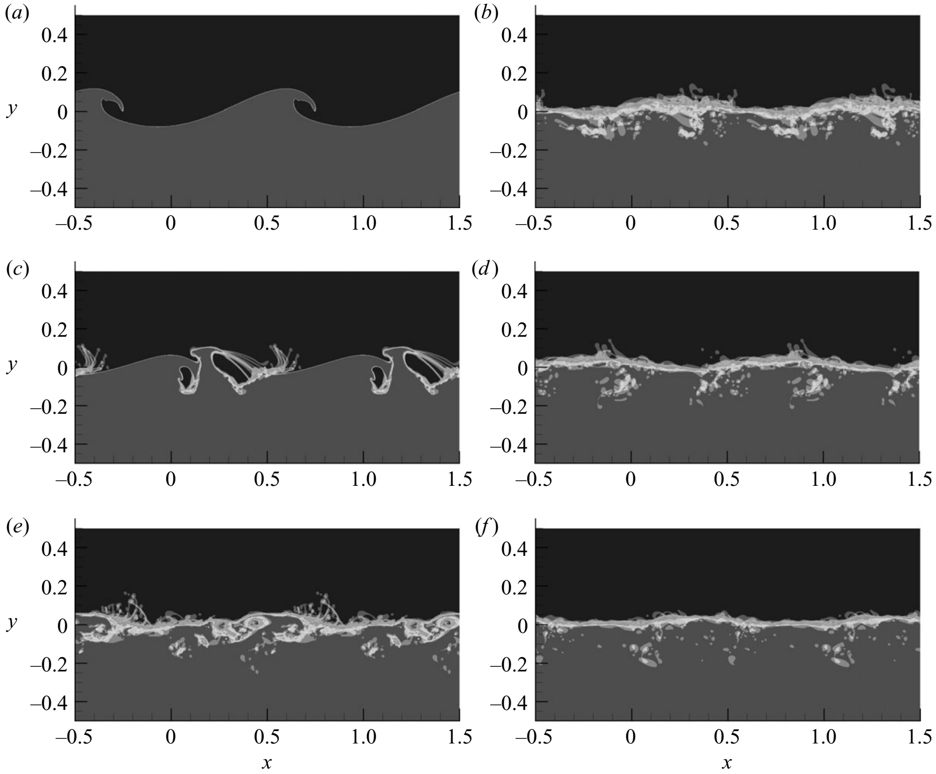

FIGURE 28. Contours of the intermittency factor $\bar{I}(\boldsymbol{x},t)$ at several time instants. From top to bottom time is $t=1, 2, 3$ and $t=4, 5, 6$ for the left and right columns, respectively.

factor is introduced as the ensemble average of an index $I(\boldsymbol{x},t)$ defined as (Brocchini & Peregrine 2001)

$$I(\boldsymbol{x},t)=\begin{cases}1 & d\geqslant 0,\\ 0 & d<0.\end{cases}$$

In figure 28 the contours of the intermittency factor $\bar{I}(\boldsymbol{x},t)$ (overbar denotes ensemble average) are drawn at several instants of time. In a linear problem, the interfaces, which are at the level $d=0$, would be simply shifted in the horizontal direction by the same amount of the initial conditions. Correspondingly, the intermittency region, i.e. the region where $0<\bar{I}(\boldsymbol{x},t)<1$, should be narrower than the cell size. Figure 28 shows that this is true up to the breaking inception only. As soon as the jet plunges onto the free surface, more relevant differences occur in terms of size and distributions of the entrapped bubbles, thus leading to a much wider intermittency area. Differences are originated by the strong nonlinearities of the flow which are triggered by the changes introduced by the peculiarities of the numerical algorithm in the treatment of the fragmentation and reconnection processes of the interface on a discrete grid. In a later stage, the large air cavity breaks into smaller ones that rise up, eventually exiting the water, and the intermittency region shrinks, although remaining remarkably larger than the grid cell.

In order to get a more quantitative understanding, in figure 29 the time history of the intermittency area is drawn. The figure shows that the intermittency area is essentially zero until the breaking onset and sharply grows after the breaking onset,

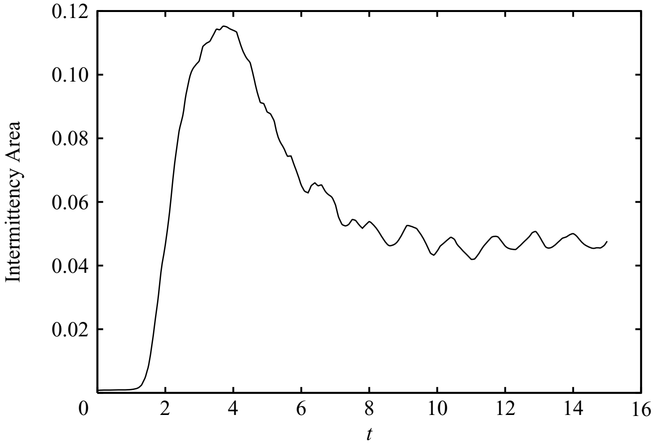

FIGURE 29. Time history of the area of the region with $0 < \bar{I}(\boldsymbol{x}, t) < 1$.

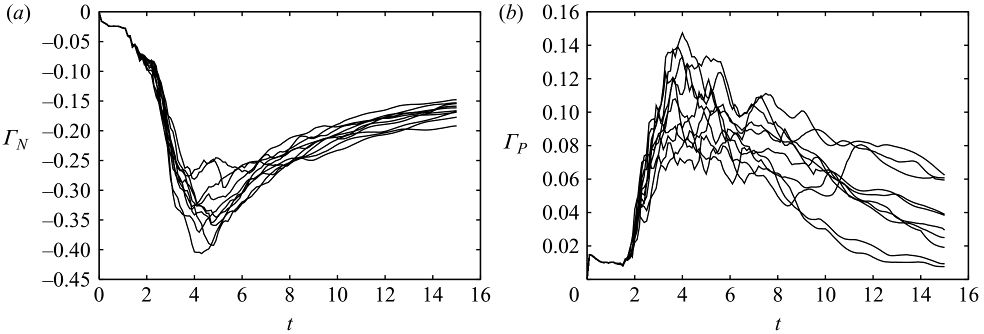

FIGURE 30. Time histories of the negative (a) and positive (b) circulations in the water domain obtained in the case $\varepsilon = 0.60$ for different values of the parameter r the initial conditions (3.3) and (3.4).

reaching its maximum at $t \simeq 3$. As the large air bubbles disappear, the intermittency area drops to about 40 % of the peak. It is interesting to note that a similar behaviour was found experimentally by Duncan (see the discussion in Iafrati 2006).

Owing to the differences in the bubble dynamics, also global quantities like energy and circulation are expected to change. In order to have a rough estimate of the corresponding uncertainty, in figure 6 the time histories of the total energy of the simulations are all drawn together. The figure shows that results are rather close to each other up to the breaking onset. Next, the total energy at a given time is scattered across a region size of which rapidly grows with time. The growth lasts up to about two fundamental wave periods after the breaking inception whereas for $t > 8$, the maximum difference between the curves is almost constant, to about 10 % of the initial energy content.

As discussed in the previous section the entrainment of air bubbles and the corresponding free-surface reconnection processes significantly affect the vorticity production in water. A quantitative estimate of the role played by small changes in the breaking dynamics can be inferred from the time histories of the positive and negative circulations shown in figure 30. The comparison between the curves in figure 30(a) indicates that the uncertainty in the negative circulation takes the largest values during the most energetic phase of the breaking process, with a maximum difference of $\Delta\Gamma \sim 0.15$. Soon after, the results become much closer to each other and the maximum difference drops to $\Delta\Gamma \sim 0.05$ and remains constant afterwards. Differently from the negative circulation, the uncertainty in the positive circulation displays a fast growth up to the most energetic phase of the breaking process and remains constant later on. It is worth remarking that although the maximum difference at the end of the numerical simulations is about the same, with $\Delta\Gamma \sim 0.05$, relatively speaking the difference is larger for the positive circulation. The above findings further support the conjecture on the basis of which the generation of the negative vorticity is strongly related to the initial conditions whereas the positive circulation, which is mostly related to the secondary entrapment of air bubbles, is more dependent on the details of the entraining process.

4. Conclusions

The unsteady wave breaking flows generated by periodic wavetrains of different amplitudes have been simulated through a two-fluids numerical approach. The study has been focused on the analysis of the role played by the breaking intensity on free-surface dynamics, air entrainment, energy dissipation, vertical transfer of momentum and vorticity.

The use of the numerical tool has allowed a direct evaluation of the viscous dissipation. In the most energetic phase of the breaking, the dissipation is seen to be localized about the entrapped air bubbles. It has been shown that the viscous dissipation, obtained as the integral of the local values, is characterized by a sharp growth soon after the breaking inception. For the numerical simulation at $Re = 10^4$, the dissipation rate in the most energetic phase of the breaking process is found to be one order of magnitude larger than that in the prebreaking stage. The most energetic phase of the breaking lasts about one-wave period. After this phase, the total dissipation decays as t^{-2}.

In order to estimate to which extent the results are affected by the low Reynolds number of the simulations, for one wave steepness the numerical simulation has been repeated using a larger Reynolds number. It has been shown that, up to about half-wave period after the breaking onset, the viscous dissipation scales with the viscosity, thus implying that the flow field in the early stage of the breaking is not strongly dependent on the Reynolds number. In the next stage, the viscous dissipation grows faster than for low Reynolds number because of the smaller structures. At that stage, however, the three-dimensional effects, neglected in the present work, become relevant.

The downward transfer of horizontal momentum has been analysed. The total flux of momentum transferred across several horizontal planes located at different depths has been evaluated and the occurrence of the surface current induced by the breaking has been highlighted. It has been shown that the amount of horizontal momentum converted into surface current grows with the breaking intensity. However, beyond a certain limit, the larger amount of air entrapped, and thus the lower value of the average density, causes a reduction in the amount of momentum transferred downward. This implies that, for large steepnesses, the layer affected by the breaking event becomes narrower. Such findings are believed to be relevant in the definition of the source term in oceanic boundary layer models.

The air entrainment and the degassing process have been described in detail. The total area of the entrapped air bubbles has been evaluated and several of the basic phenomena have been qualitatively described on the basis of the free-surface profiles. It has been shown that the area of the air cavity entrapped by the plunging jet at the onset of breaking grows with the initial steepness as ε^7. A further investigation is needed to evaluate to which extent this result depends on the initial conditions adopted here.

The vorticity field induced in water by the breaking process has been carefully analysed. A distinction has been made between the circulations associated to the negative and positive vorticities. It has been shown that, in the spilling breaking case, vorticity is mainly generated by viscous effects taking place at the toe of the bulge. In the plunging breaking case, the reconnection process has been found to be a much more efficient mechanism of vorticity generation. It has been shown that the circulation induced by the first plunging event scales with the crest-to-trough velocity jump. In the most energetic phase of the breaking process, i.e. the phase with the largest amount of entrapped air, the ratio is about 0.3–0.5. At least up to half-wave period after the breaking onset, the primary circulation is almost independent of the Reynolds number.

With the aim of estimating the uncertainty in the numerical results, several repetitions of the same simulation have been done introducing a small perturbation to the initial conditions. It has been shown that the primary circulation is rather repeatable whereas, relatively speaking, a larger uncertainty characterizes the secondary circulation, thus indicating that the latter is more dependent on the details of the bubble entrainment process. In addition to the total circulations, the uncertainty in the free-surface location has been evaluated. It has been found that results are rather repeatable up to the breaking inception, with the size of the uncertainty region comparable to the initial perturbation. As soon as the breaking develops, the strong nonlinearities of the problem induce a much larger scatter in the free-surface location. The intermittency area undergoes a sharp growth and takes the maximum values in the most energetic phase of the breaking process. In the next stage, when the largest air bubbles disappear, the region of intermittency shrinks and the total area diminishes up to a constant value about 40 % of the peak.

The author thanks Professor J. H. Duncan and Professor K. P. Melville for the useful suggestions provided during the preparation of the manuscript. The author expresses sincere gratitude to the two anonymous reviewers for their useful comments and suggestions. This work has been done in the framework of the *Programma Ricerche INSEAN 2007–2009* financially supported by the Italian *Ministero dei Trasporti.*

REFERENCES

Banner, M. L. & Phillips, O. M. 1974 On the incipient breaking of small scale waves. *J. Fluid Mech.* **65**, 647–656.

Blenkinsopp, C. E. & Chaplin, J. R. 2007 Void fraction measurements in breaking waves. *Proc. R. Soc.* A**463**, 3151–3170.

Bonmarin, P. 1989 Geometric propertiesd of deep-water breaking waves. *J. Fluid Mech.* **209**, 405–433.

Brackbill, J. U., Kothe, D. B. & Zemach, C. 1992 A continuum method for modeling surface tension. *J. Comput. Phys.* **100**, 335–354.

Brocchini, M. & Peregrine, D. H. 2001 The dynamics of strong turbulence at free surfaces. Part 1. Description. *J. Fluid Mech.* **449**, 225–254.

Chang, K.-A. & Liu, P. L.-F. 1999 Experimental investigation of turbulence generated by breaking waves in water of intermediate depth. *Phys. Fluids* **11**, 3390–3401.

Chen, G., Kharif, C., Zaleski, S. & Li, J. 1999 Two-dimensional Navier–Stokes simulation of breaking waves. *Phys. Fluids* **11**, 121–133.

Chorin, A. J. 1967 A numerical method for solving incompressible viscous flow problems. *J. Comput. Phys.* **2**, 12–26.

Dabiri, D. & Gharib, M. 1997 Experimental investigation of the vorticity generation within a spilling water wave. *J. Fluid Mech.* **330**, 113–139.

Deane, G. B. & Stokes, M. D. 2002 Scale dependence of bubble creation mechanisms in breaking waves. *Nature* **418**, 839–844.

Diorio, J., Liu, X. & Duncan, J. H. 2008 On the self-similarity of short-wavelength incipient spilling breakers. In *Proceedings of the XXII ICTAM Conference*, University Adelaide.

Duncan, J. H. 1981 An experimental investigation of breaking waves produced by a towed hydrofoil. *Proc. R. Soc. Lond.* A**377**, 331–348.

Duncan, J. H. 1983 The breaking and nonbreaking wave resistance of a two-dimensional hydrofoil. *J. Fluid Mech.* **126**, 507–520.

Duncan, J. H., Qiao, H., Philomin, V. & Wenz, A. 1999 Gentle spilling breakers: crest profile evolution. *J. Fluid Mech.* **379**, 191–222.

Frisch, U. 1995 *Turbulence*. Cambridge University Press.

Grue, J., Clamond, D., Huseby, M. & Jensen, A. 2003 Kinematics of extreme water waves. *Appl. Ocean Res.* **25**, 355–366.

Grue, J. & Fructus, D. In press Model for fully nonlinear ocean wave simulations derived using Fourier inversion of integral equations in 3D. In *Advances in Numerical Simulation of Nonlinear Water Waves* (ed. Q. W. Ma), in the series of Advances in Coastal and Ocean Engineering . The World Scientific.

Grue, J. & Jensen, A. 2006 Experimental velocities and accelerations in very steep wave events in deep water. *Eur. J. Mech. B Fluids* **25**, 554–564.

Hendrickson, K. 2004 Navier–Stokes simulation of steep breaking water waves with coupled air–water interface. Sc. D. Dissertation, Massachussetts Institute of Technology.

Hendrickson, K. & Yue, D. K. P. 2006 Navier–Stokes simulations of unsteady small-scale breaking waves at a coupled air–water interface. In *Proceedings of The Twenty-Sixth Symposium on Naval Hydrodynamics*, Office of Naval Research.

Iafrati, A. 2006 Numerical analysis of the momentum transfer induced by breaking waves. In *Proceedings of The Twenty-Sixth Symposium on Naval Hydrodynamics*, Office of Naval Research.

Iafrati, A. & Campana, E. F. 2003 A domain decomposition approach to compute wave breaking. *Intl J. Num. Meth. Fluids* **41**, 419–445.

Iafrati, A. & Campana, E. F. 2005 Free surface fluctuations behind microbreakers: space–time behavious and subsurface flow field. *J. Fluid Mech.* **529**, 311–347.

Iafrati, A., Di Mascio, A. & Campana, E. F. 2001 A level-set technique applied to unsteady free surface flows. *Intl J. Num. Meth. Fluids* **35**, 281–297.

Kim, J. & Moin, P. 1985 Application of a fractional-step method to incompressible Navier–Stokes equations. *J. Comput. Phys.* **59**, 308–323.

Kimmoun, O. & Branger, H. 2007 A particle image velocimetry investigation on laboratory surf-zone breaking waves over a sloping beach. *J. Fluid Mech.* **588**, 353–397.

Lamarre, E. & Melville, W. K. 1991 Air entrainment and dissipation in breaking waves. *Nature* **351**, 469–472.

Landau, L. D. & Lifshitz, E. M. 1959 *Fluid Mechanics*. Pergamon.

Lighthill, J. 1978 *Waves in Fluids*. Cambridge University Press.

Lin, J. C. & Rockwell, D. 1995 Evolution of a quasi-steady breaking wave. *J. Fluid Mech.* **302**, 29–44.

Longuet-Higgins, M. S. 1992 Capillary rollers and bores. *J. Fluid Mech.* **240**, 659–679.

Lubin, P., Vincent, S., Abadie, S. & Caltagirone, J.-P. 2006 Three-dimensional large eddy simulation of air entrainment under plunging breaking waves. *Coast. Engng* **53**, 631–655.

Melville, W. K., Veron, F. & White, C. J. 2002 The velocity field under breaking waves: coherent structures and turbulence. *J. Fluid Mech.* **454**, 203–233.

Ohring, S. & Lugt, H. J. 1991 Interaction of a viscous vortex pair with a free surface. *J. Fluid Mech.* **227**, 47–70.

Qiao, H. & Duncan, J. H. 2001 Gentle spilling breakers: crest flow-field evolution. *J. Fluid Mech.* **439**, 57–85.

Rai, M. M. & Moin, P. 1991 Direct simulations of turbulent flow using finite-difference schemes. *J. Comput. Phys.* **96**, 15–53.

Rapp, R. J. & Melville, W. K. 1990 Laboratory measurements of deep-water breaking waves. *Phil. Trans. R. Soc. Lond.* A**331**, 735–800.

Rosenfeld, M., Kwak, D. & Vinokur, M. 1991 A fractional step solution method for the unsteady incompressible Navier–Stokes equations in generalized coordinate system. *J. Comput. Phys.* **94**, 102–137.

Sarpkaya, T. & Suthon, P. 1991 Interaction of a vortex couple with a free surface. *Exp. Fluids* **11**, 205–217.

Scardovelli, R. & Zaleski, S. 1999 Direct numerical simulation of free surface and interfacial flow. *Ann. Rev. Fluid Mech.* **31**, 567–603.

Siddiqui, M. H. K., Loewen, M. R., Asher, W. E. & Jessup, A. T. 2004 Coherent structures beneath wind waves and their influence on air–water gas transfer. *J. Geophys. Res.* **109**, C03024.

Siddiqui, M. H. K., Loewen, M. R., Richardson, C., Asher, W. E. & Jessup, A. T. 2001 Simultaneous particle image velocimetry and infrared imagery of microscale breaking waves. *Phys. Fluids* **13**, 1891–1903.

Song, C. & Sirviente, A. I. 2004 A numerical study of breaking waves. *Phys. Fluids* **16**, 2649–2667.

Sullivan, P. P., McWilliams, J. C. & Melville, W. K. 2004 The oceanic boundary layer driven by wave breaking with stochastic variability. Part 1: Direct numerical simulations. *J. Fluid Mech.* **507**, 143–174.

Sullivan, P. P., McWilliams, J. C. & Melville, W. K. 2007 Surface gravity wave effects in the oceanic boundary layer: large-eddy simulation with vortex force and stochastic breakers. *J. Fluid Mech.* **593**, 405–452.

Sussman, M., Smereka, P. & Osher, S. 1994 A level set approach for computing solutions to incompressible two-phase flow. *J. Comput. Phys.* **114**, 146–159.

Thorpe, S. A. 2004 Langmuir circulation. *Ann. Rev. Fluid Mech.* **36**, 55–79.

Unverdi, S. O. & Tryggvason, G. 1992 A front-tracking method for viscous, incompressible, multi-fluid flows. *J. Comput. Phys.* **100**, 25–37.

van der Vorst, H. A. 1992 Bi-CGSTAB: fast and smoothly converging variant of Bi-CG for the solution of nonsymmetric linear systems. *SIAM J. Sci. Stat. Comput.* **13**, 631–644.

Watanabe, Y., Saeki, H. & Hosking, R. J. 2005 Three-dimensional vortex structures under breaking waves. *J. Fluid Mech.* **545**, 291–328.

Whitham, G. B. 1974 *Linear and Nonlinear Waves*. Wiley Interscience.

Zang, Y., Street, R. L. & Koseff, J. R. 1994 A non-staggered grid, fractional step method for time-dependent incompressible Navier–Stokes equations in curvilinear coordinates. *J. Comput. Phys.* **114**, 18–33.